Mid-Latitude Climatologies of Mesospheric Temperature and Geophysical Temperature Variability Determined with the Rayleigh-Scatter Lidar at ALO-USU

Joshua P. Herron[1,2] and Vincent B. Wickwar[1,3]

[1]Atmospheric Lidar Observatory, Center for Atmospheric and Space Science, Utah State University, Logan, UT, USA

[2]Space Dynamics Laboratory, Logan, UT, USA

[3]Physics Department, Utah State University, Logan, UT, USA

Correspondence to: Vincent B. Wickwar, Center for Atmospheric and Space Sciences, Utah State University, 4405 Old Main Hill, Logan, UT 84322-4405; vincent.wickwar@gmail.com

Key Points:

- Climatologies of mesospheric temperature and their geophysical variability from 11 years of USU Rayleigh lidar observations are presented
- Significant features in both: October "cold island", January "cold valley", 170 K mesopause, seasonal variability decreasing with altitude
- These climatologies compare well to those from the French and Canadian, mid-latitude (40° to 45° N), Rayleigh lidars

Short Title: Rayleigh lidar temperature and variability climatologies

Abstract

From 1993-2004, 839 nights were observed with the Rayleigh-scatter lidar at Utah State University's Atmospheric Lidar Observatory. They were reduced to obtain nighttime mesospheric temperatures between 45 and ~90 km, which were then combined to derive composite annual climatologies of mid-latitude temperatures and geophysical temperature variability. At 45 km, near the stratopause, there is a ~250 K temperature minimum in mid-winter and a 273 K maximum in mid-May. The variability behaves oppositely, being 7-10 K in winter and 2.5 K in summer. At 85 km, there is a 215 K temperature maximum at the end of December and a 170 K mesopause minimum in early June. In contrast, the variability is roughly constant at ~20 K. -At both low and high altitudes, the temperatures change much more rapidly in spring than in fall. The transition between these opposite temperature behaviors is 65 km. Distinctive temperature structures occur in all regions. In mid-winter, between 45 and 50 km, a 6 K warm region appears, most likely from occasional sudden stratospheric warmings. Above that, a "cold valley" extends to 70 km, which may be related to the bottom side of intermittent inversion layers. Both regions have increased variability. Near 85 km, there is a very rapid heating event of 25 K/month in August with high variability. In October, a temperature minimum, a "cold island", occurs from 78–86 km with low variability, indicating a regular feature. These USU results are compared extensively to those from other mid-latitude lidars in Canada and France.

Plane Language Summary

We present the results from 11 years of observations of the mesosphere, the 45-90 km portion of the middle atmosphere. We used a Rayleigh lidar, a radar-like system that uses pulses of light that are backscattered from atmospheric molecules. We obtained good data from 839 nights above northern Utah. From these, we derived altitude profiles of neutral temperature. We combined these profiles to construct climatologies of how the temperatures evolve day-by-day during the year and how much they can vary on a given day. As expected, in the lower mesosphere, the summer was warmer than the winter. In addition, the winter had much greater variability, indicating the likely contribution of competing, time-varying, geophysical heating and cooling processes. But, in the upper mesosphere, the summer was much colder than the winter. The coldest temperatures occurred in June at the mesopause, which we found to be 170 K at 85 km. In contrast, the mid-winter temperature was 45 K warmer. While the variability at these higher altitudes was much greater because fluctuations grow with altitude, it was almost constant throughout the year. Comparisons with data from French and Canadian Rayleigh lidar groups that observe at similar latitudes found very similar results.

1. Introduction

The temperature structure of the atmosphere is a very distinctive feature, serving as the basis for defining the different atmospheric regions. The temperature climatology provides fundamental information about the energetics of these regions and serves as a reference for evaluating first-principle models. It is also a reference for detecting and exploring unusual events or phenomena. Regular measurements of much of the middle atmosphere were very difficult prior to the advent of Rayleigh-scatter lidar. Balloons, which are used in the troposphere and stratosphere, typically reach altitudes less than 30 km. Likewise, special high-flying aircraft have a similar altitude ceiling. Resonance lidar observations only begin above 80 km. Airglow observations only begin above 85 km. Rocket soundings are infrequent because of their expense. Until recently, satellite remote-sensing observations had poor altitude resolution and, in any case, are unable to provide time evolution above selected locations. Rayleigh-scatter lidar observations (Hauchecorne and Chanin, 1980) changed this situation. Regular mid-latitude observations between 40° and 45° N latitude throughout most of the mesosphere have been undertaken by the French (Hauchecorne et al., 1991; Keckhut et al., 1993; Leblanc et al., 1998) since 1978, by our group (Wickwar et al., 1997; Beissner, 1997; Wickwar et al., 2001; Herron, 2004, 2007) from 1993 through 2004, and by the Canadians (Sica et al., 1995; Argall and Sica, 2007; Jalali et al., 2016) since 1993. Observations have also been carried out in other latitude regions. For instance, at a higher latitude, 54.1° N, the Germans have been making such observations since 2002 (Gerding et al., 2008). And, at lower latitudes, 34.4° N and 19.5° N, the lidar group from the Jet Propulsion Laboratory has been making such observations since 1990 and 1993, respectively (Leblanc et al., 1998). Such frequent, long-term measurements are necessary for exploring this region and for producing good climatologies of temperature and temperature variability. As of 2004, our data set, based on 5972 hours from 964 nights of Rayleigh lidar observations spanning 11 years, was one of the longest data sets in the 40°–45° mid-latitude region and one of the densest from that period. In this paper, we present the mesospheric temperature composite annual climatology between 45 and approximately 90 km above the Atmospheric Lidar Observatory (ALO) on the campus of at Utah State University (USU) in Logan, Utah (ALO-USU). We also present the climatology of the composite geophysical temperature variability. The significance of these climatologies are, above all, to provide a background against which theory and model calculations can be compared to see if the effects of radiation, winds, waves, and chemistry are properly understood. In addition, they provide a reference against which to compare temperatures from various subsets of the data to look for unusual or special conditions, and a reference to make comparisons with other climatologies to investigate longitudinal and latitudinal differences. Besides presenting these two climatologies, this paper sets the stage for subsequent papers that will examine the data in other ways and make comparisons with other data sets and models. The lidar and data reduction are described in Section 2, the observations are presented in Section 3, they are discussed in Section 4 along with comparisons to other mid-latitude lidars, and the summary and conclusions are given in Section 5.

2. Description of the Lidar and Data Reduction

The original Rayleigh-scatter lidar operated on the USU campus at ALO-USU (41.74°N, 111.81°W, and 1466 m), which is part of the Center for Atmospheric and Space Sciences (CASS), from August 1993 through December 2004. The lidar consisted of a frequency-doubled Nd:YAG laser operated at 532 nm with a repetition rate of 30 Hz. During this period two lasers were used at different times: one had an average power of 18 W, the other 24 W. The laser was Q-switched, providing a short pulse of ~7 ns. The backscattered light was collected by a 44-cm diameter Newtonian telescope, which gave a system power-aperture product of 2.7 or 3.6 Wm^2, depending on the laser. The telescope focused the backscattered light onto a field stop at the prime focus, giving a field of view approximately 3 times that of the 0.5 mrad laser divergence. Its light then passed through a field lens to another lens that focused the light onto the plane of a mechanical chopper. Another lens collimated that light and passed it through a narrow-band, high-transmittance interference filter (1 nm and 80%) and into a cooled photomultiplier tube (PMT) housing (Products for Research) that held a green-sensitive, bi-alkali PMT (Electron Tubes 9954). The narrow, high-transmittance filter and cooled PMT housing helped extend the acquisition of good data to as high an altitude as possible. The 1466-m altitude of ALO also helped in that regard. The basic altitude resolution was 37.5 m, corresponding to a range bin of 250 ns. The returns from 3600 pulses were summed before they were recorded to disk, giving a minimum time resolution of 2 minutes. The data can be integrated afterwards in the data reduction in both altitude and time. For this study, they were integrated over 3 km in altitude and all night in time. However, the calculations were still carried out every 37.5 m. Most of the observations started approximately an hour after sunset and ended approximately an hour before dawn. The intent was to make all-night observations. However, because of clouds, on some nights the observations ended early and on roughly an equal number of nights they started late. A more detailed description of the lidar is given elsewhere (Beissner, 1997; Wickwar et al., 2001; Herron, 2004, 2007).

The lidar signal is composed of backscattered photons, background photons, and dark counts. To protect the PMT from large, low-altitude signals, a mechanical chopper blocked most of the return from below 20 km, and electronic gating in the PMT reduced the gain by about a factor of 700 below 38 km. We appeared to obtain better PMT behavior when using both the chopper and electronic gating. Good data after the gate turn-on were acquired starting at approximately 41 km. This relatively high altitude also ensured that the PMT count rate was in its linear range, which was essential for deriving good temperatures. At and above this altitude, possible extinction by stratospheric aerosols (Hauchecorne et al., 1991) and absorption by O_3 (Sica et al., 2001) can be neglected. At higher altitudes, there is the possibility of Mie scattering from ice crystals in noctilucent clouds (Wickwar et al., 2002; Herron et al., 2007), but they occur rarely at this latitude and stand out clearly in the return signal. Consequently, the altitude-dependent signal above 41 km is effectively due only to Rayleigh scattering. The returns are measured out to an altitude of 525 km. Extended regions between 120 and 350 km can be used to enable both an accurate and precise determination of the background signal and, on occasion, to provide a diagnostic tool for the detector system. Once a suitable background level is determined and subtracted, the signal is corrected for the inverse range-squared falloff of the return signal. The resulting profile is proportional to molecular density and is integrated downward to determine profiles of absolute temperature by assuming the atmosphere is in hydrostatic equilibrium and obeys the ideal gas law (Hauchecorne and Chanin, 1980; Beissner, 1997; Herron, 2004). To do this, we need the mean molecular mass. Because the downward integration begins at or below 95 km, it is assumed that turbulent mixing leads to a constant mean molecular mass based on 78.1% N_2, 20.9% O_2, and 0.93% Ar (Goody and Yung, 1989). We also need the gravitational acceleration normal to the geoid as a function of altitude. We used the very detailed formulation provided by NIMA (2000). A major strength of the Rayleigh lidar technique is that the temperature profiles are independent of time variations in the atmospheric transmittance (mostly arising from thin clouds and aerosols) and laser power. The temperatures do not have to be calibrated. However, they do depend on very good observational and data reduction procedures. More generally, a detailed discussion of the analysis procedure and its verification using extensive simulations is given in Herron (2004).

To calculate the absolute temperature, an a priori knowledge of the temperature at the start of the downward integration is necessary. The initial values were taken from the 8-year climatology from the sodium lidar at Colorado State University (CSU) (She et al., 2000), which was only 575 km away and just over 1° equatorward of ALO-USU. The CSU temperatures were from 1990 to 1999, covering much of the same time period as the ALO-USU data. The use of this nearby climatology in deriving our Rayleigh climatology should be more appropriate than using an empirical model such as NRLMSISe-00 (Picone et al., 2002). However, because of the existence of large amplitude temperature waves, with amplitudes as great as 20 K, that we identified in a noctilucent cloud study (Herron et al., 2007), a climatological initial temperature could still have a large error, too high or too low, at the highest altitudes for a given night. But, averaging together the many nights that go into our composite climatology minimizes the effect of these and other waves at the highest altitudes. At lower altitudes, these initial values are not significant because any systematic error from this initial temperature decreases rapidly with the downward integration because of the exponentially increasing density. For instance, using a neutral-density scale height of 7 km, any difference between the derived and actual temperatures decreases by a factor of ~4 after 10 km of integration and by a factor of ~17 after 20 km. Thus, the Rayleigh temperatures become independent of the initial values after a relatively short distance.

The starting altitude for the downward temperature integration is determined as the altitude at which the signal is 20 times its standard deviation, or a 5% uncertainty in the signal. This implies a 5% uncertainty in the number density. This, in turn, leads to a 6% temperature uncertainty. The average starting altitude for nighttime temperature profiles is 87 km, but even for the very best data the maximum altitude was capped at 95 km. The use of the CSU climatology for the starting values and the averaging of many nights, coupled with the rapid decrease of any initial errors, should ensure that accurate temperatures are obtained for altitudes below 80 km and that reasonably accurate temperatures are obtained significantly above 80 km all the way to the maximum altitude.

At the upper limit of the lidar's data range, the background becomes a large portion of the total signal. Its accurate determination at a yet higher altitude, in the region above 120 km, is most important for the data reduction. In that region, it should be constant. Typically, the background was estimated by averaging the signal between 120 and 170 km. Occasionally it was averaged over slightly different ranges. The accuracy is important because a bad background can lead to systematic temperature errors at all altitudes (Herron, 2004). Observationally, bad backgrounds can have positive or negative slopes, oscillations, or spikes. While not common, these bad behaviors indicated that either equipment was failing or that improper settings had been used. Experimentation with simulated data also showed that significantly too high or too low an estimated background would lead to temperatures that increased or decreased sharply immediately below the initial altitude, thus warning of a potential problem. The effects of random small variations in the observed background level on the deduced temperatures are reduced by the subsequent averaging of many nights to produce the climatology. On some nights, mostly because of clouds, the signal strength was too small to obtain good temperatures. Between 1993 and 2004 observations were obtained on 964 nights covering 5972 hours. Of these, 839 nights covering 5273 hours were of such quality as to give good temperatures. The monthly distributions of nights and hours observed that contributed to the two composite climatologies are given in Figure 1.

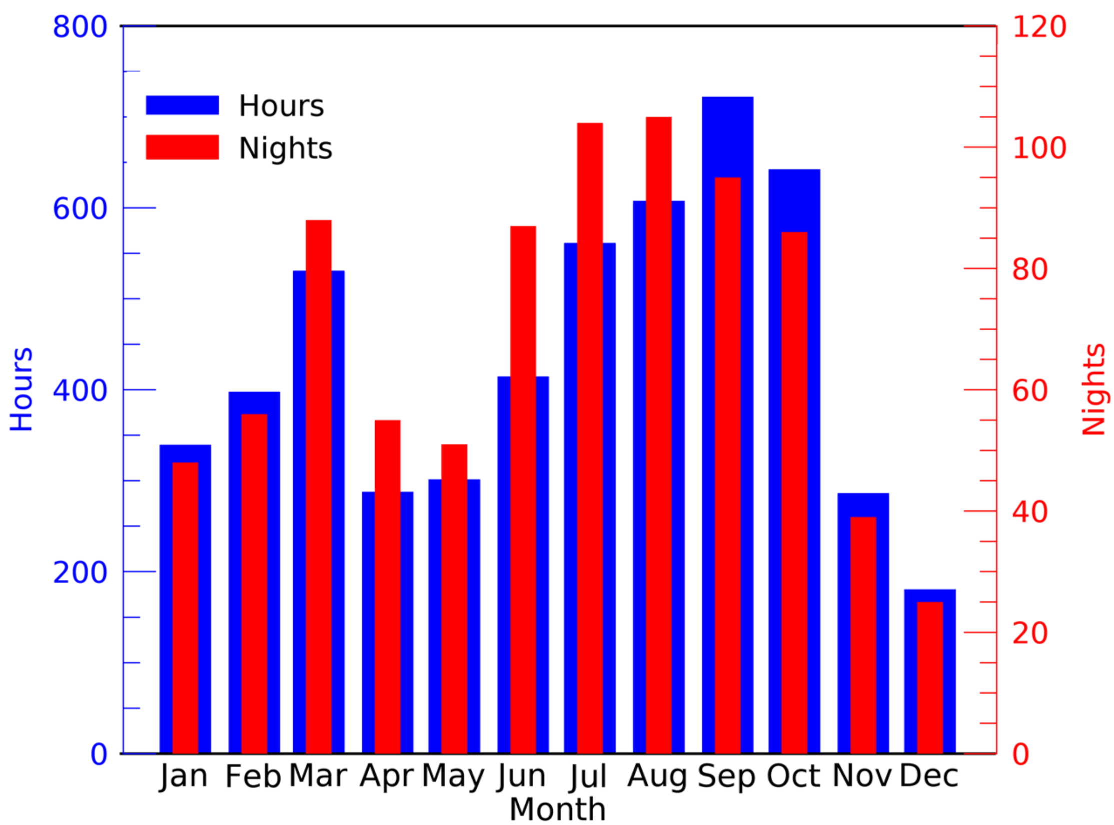

Figure 1. Number of Good Nights and Hours Observed Each Month in the ALO-USU Composite Year. The good nights are in red, the hours in blue.

An average temperature profile is found for each night of a composite year by averaging the nighttime temperature profiles over a 31-day by 11-year window centered on that night. Because each of the nighttime profiles included in the average can have a different starting altitude, the maximum altitude for the average is dependent on the distribution of these starting altitudes. The averaging starts at 45 km with the maximum (or close to the maximum) number of profiles in the averaging window and continues upward until half of the maximum number remains. (Occasionally the number of profiles increases over the first few km because the electronic gate had been set too high, giving the maximum number at a slightly higher altitude.) Seventy-five percent of the individual nighttime temperature profiles have their maximum altitude, the starting altitude for the downward integration, between 84 and 95 km. The average altitude for all the individual nights in the dataset is ~87 km. As might be expected, after the multi-night by multi-year averaging, the maximum altitude in the climatological averages is almost the same, 88 km. This also implies that half the nights in the averages start above 88 km. As seen from the individual profiles in Figure 2, many reached 95 km.

After finding the temperatures, the next important question concerns their significance and variability. The starting point is the Poisson uncertainty from photon counting. Its effect on the derived temperature uncertainty and, hence, variance has been given by Gardner (1989), Beissner (1997), and Herron (2004, 2007). Provided these temperature variances are fairly similar at a given altitude from night to night, which they should be, they can be averaged over the same 31-day by 11-year window as the signal to find the average temperature variance,

$$\sigma_T^2(h) = [1/N(h)] \sum_{i=1}^{N(h)} \sigma_i^2(h) \qquad (1)$$

where $\sigma_i^2(h)$ is the temperature variance for the ith night at altitude h, and $N(h)$ is the total number of nights in the averaging window at that altitude. This variance can be divided by $N(h)$ to find the variance of the mean temperature $\bar{T}(h)$. The square root of that gives the standard deviation of the temperature uncertainty,

$$\sigma_{\bar{T}}(h) = \sqrt{\sigma_T^2(h)/N\,(h)}\,. \qquad (2)$$

This is a good estimate of the contribution to the uncertainty of the mean temperature arising from the Poisson uncertainty from photon counting, provided all the temperatures in the averaging window are from the same temperature distribution.

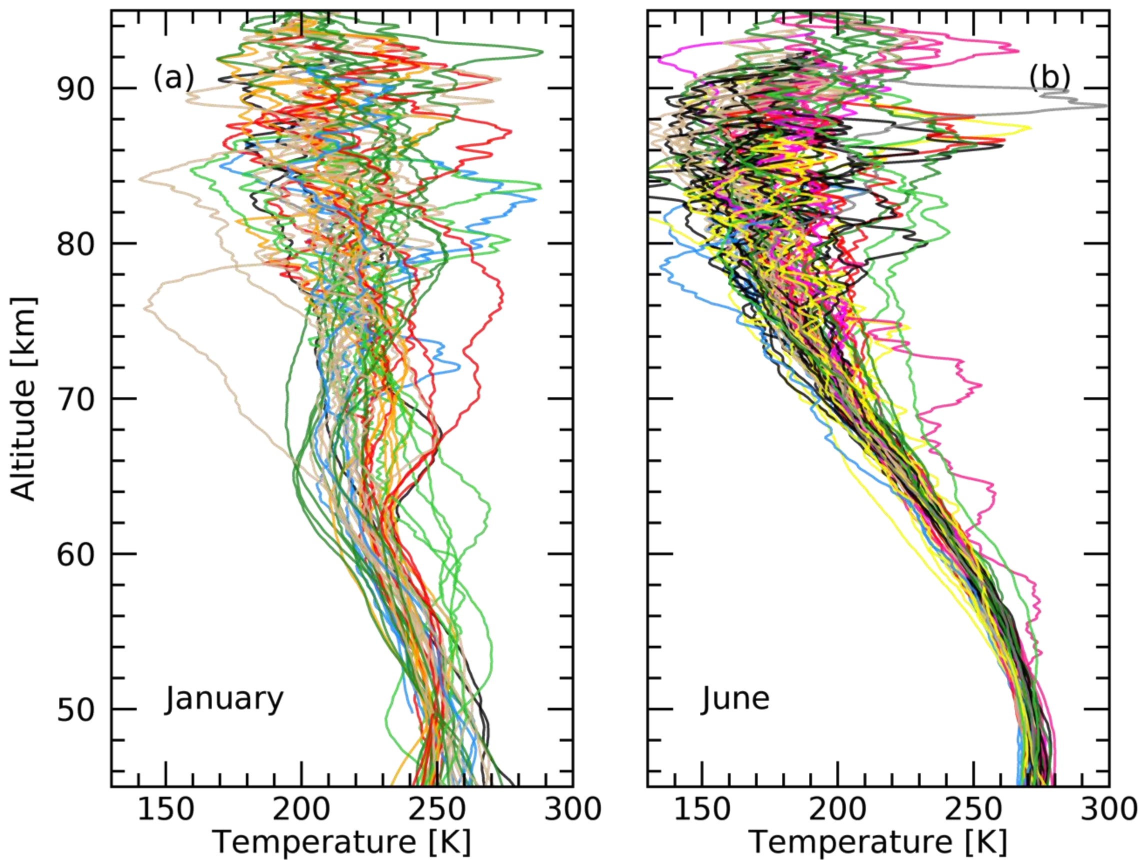

Figure 2. Superposition of Individual Nighttime Temperature Profiles from January and June, the Extreme Winter and Summer Months. Nighttime temperature profiles from (a) all 48 January and (b) all 87 June observations. A different color is used for each year. These are examples of two of the ensemble of profiles that contribute to the 31-day by 11-year averages shown in Figure 5. The standard deviations of the mean $s_{\bar{T}}(h)$ used in Figure 3 and shown in Figures 4 and 6 are calculated from such ensembles of profiles.

However, much greater temperature variability arises because of day-to-day and year-to-year geophysical temperature variability, $\sigma_{Geo}(h)$. The combined effects of measurement uncertainty from Poisson counting statistics and geophysical temperature variability is found from the sample variance,

$$s_T^2(h) = \{1/[N(h) - 1]\} \sum_{i=1}^{N(h)} [T_i(h) - \bar{T}(h)]^2 \tag{3}$$

where $T_i(h)$ is the *i*th derived temperature and $\bar{T}(h)$ is the average of the $T_i(h)$, and $N(h)$ is the total number of nights in the averaging window at altitude h. This sample variance can also be divided by $N(h)$ to estimate the variance of $\bar{T}(h)$. The square root of that gives the standard deviation of the total temperature uncertainty from the combined effects of the Poisson counting statistics and geophysical variability,

$$s_{\bar{T}}(h) = \sqrt{s_T^2(h)/N(h)}\,. \tag{4}$$

As such, it indicates the significance of the derived mean temperature $\bar{T}(h)$. It provides the temperature uncertainties of the mean (error bars) for the temperatures shown in Figure 3, the uncertainty profiles shown in Figure 4 for the temperatures in Figure 5, and the uncertainty profiles (solid lines) shown in Figure 6 for the January and June temperatures. These are discussed in the next Section.

In addition to $s_T(h)$ giving the standard deviation for the temperature distribution, it can be combined with the Poisson-derived temperature uncertainty $\sigma_T(h)$ to determine the geophysical temperature uncertainty or variability,

$$\sigma_{Geo}(h) = \sqrt{s_T^2(h) - \sigma_T^2(h)}\,. \tag{5}$$

This formulation is consistent with that of Leblanc et al. (1998) and Argall and Sica (2007). It is used to find the composite climatology of the geophysical temperature variability, which changes significantly with time during the year and with altitude, reflecting changes and evolution in the underlying physical processes. The 31-day by 11-year integration is long enough that it is not sensitive to variations from gravity waves. The waves that could affect this average have periods that range from 2 to 31 days. Contours of $\sigma_{Geo}(h)$ for the composite-year temperature variability are shown in Figure 7.

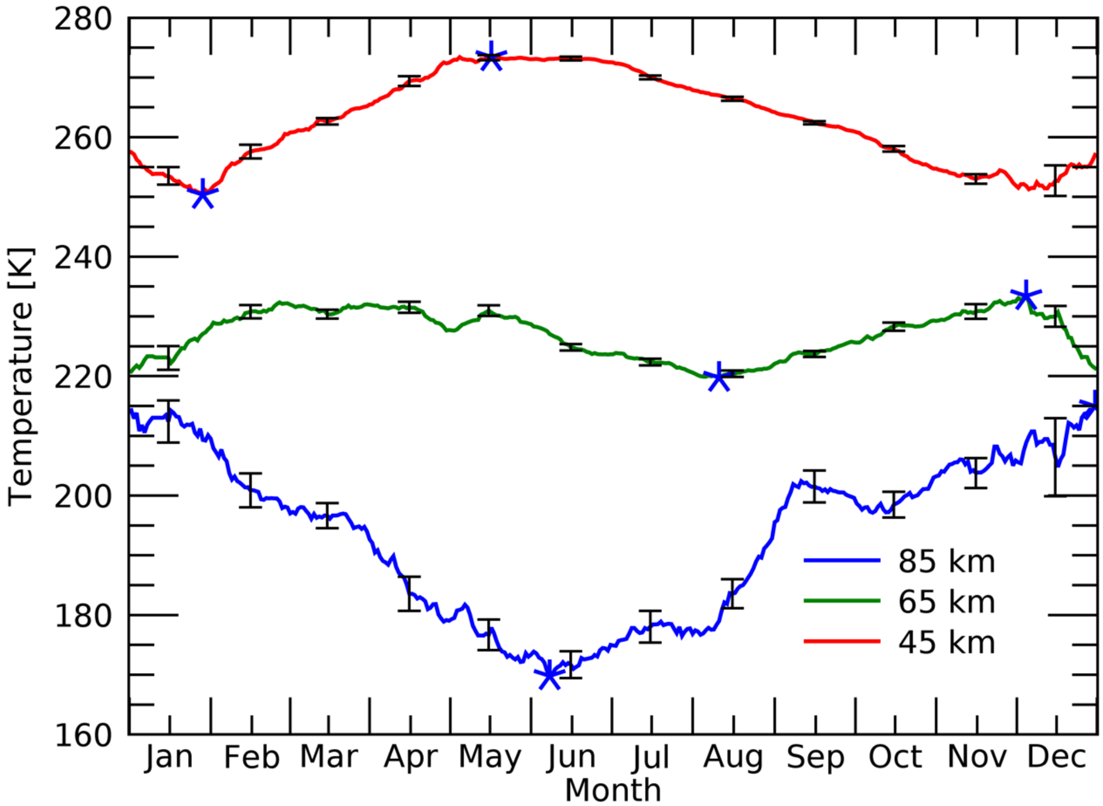

Figure 3. ALO-USU Climatological Nighttime Temperatures $\overline{T}$ at 45, 65, and 85 km. The temperatures are averaged over a 31-day by 11-year window centered on each night of the composite year. The error bars are from the standard deviation of the mean $s_{\overline{T}}(h)$ given at the three altitudes by Equation 4 and shown as profiles in Figure 4. The ☆ symbol marks maximum and minimum temperatures.

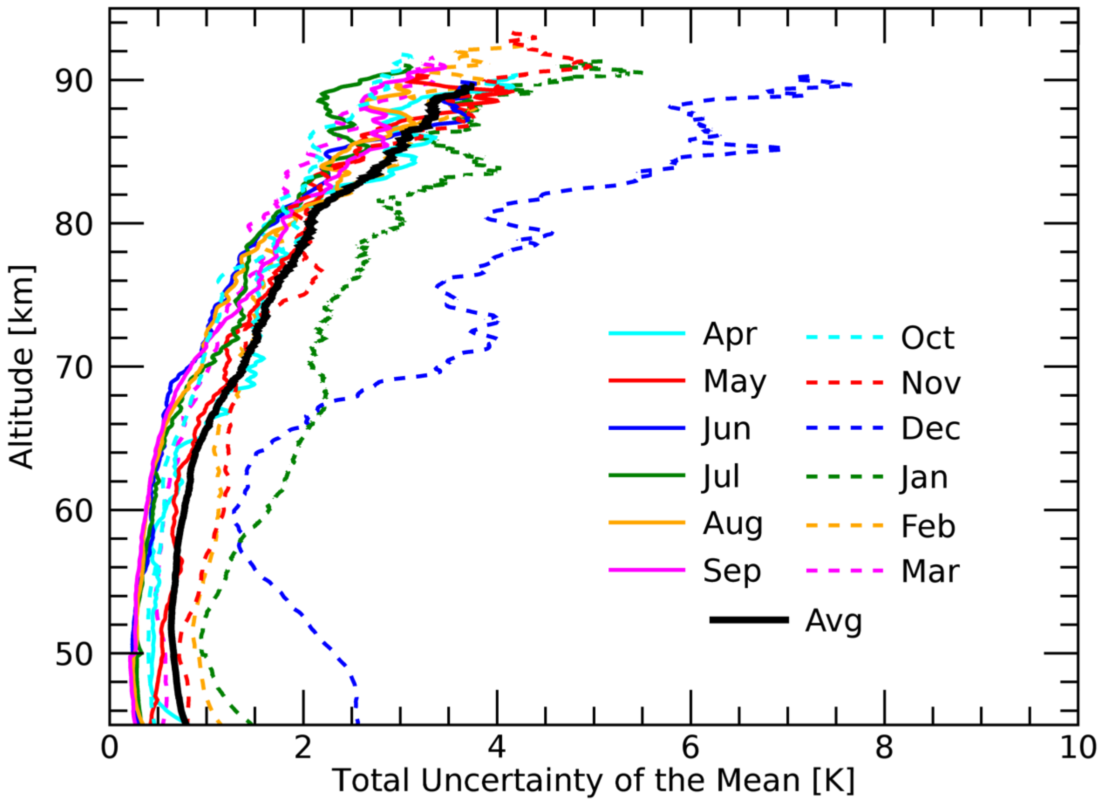

Figure 4. Mid-month Profiles of Standard Deviations of the Mean $s_{\bar{T}}(h)$ for the ALO-USU Climatology of Nighttime, Mesospheric Temperatures. There is a profile for each mid-month mean temperature profile $\bar{T}(h)$ shown in Figure 5. These standard deviations include the effects from both Poisson statistics and geophysical variability. The solid profiles are for April through September and the dashed profiles are for October through March. The black curve is the average annual temperature uncertainty profile obtained by averaging the twelve, one-month profiles.

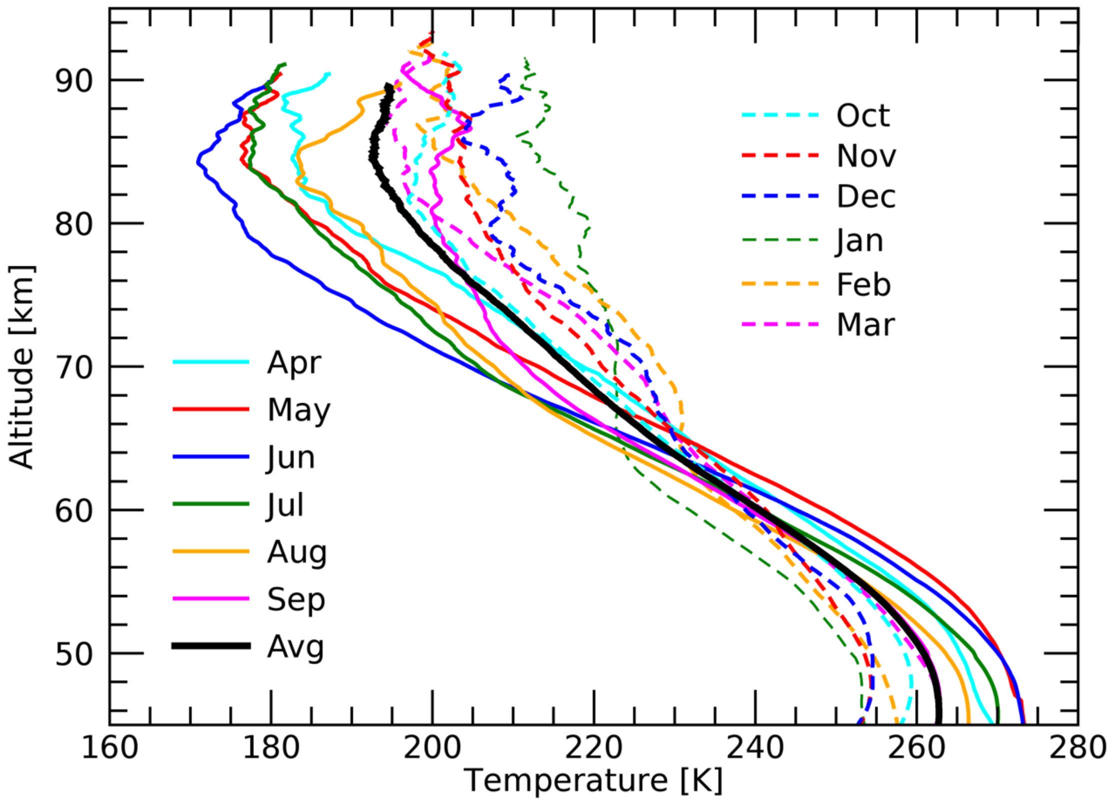

Figure 5. Mid-month Temperature Profiles $\overline{T}(h)$ from the ALO-USU Climatology of Nighttime, Mesospheric Temperatures. The temperatures are averaged over a 31-day by 11-year window centered on the middle of each month of the composite year. The solid profiles are for April through September and the dashed profiles are for October through March. The heavy black curve is the average annual temperature profile obtained by averaging the twelve, one-month profiles.

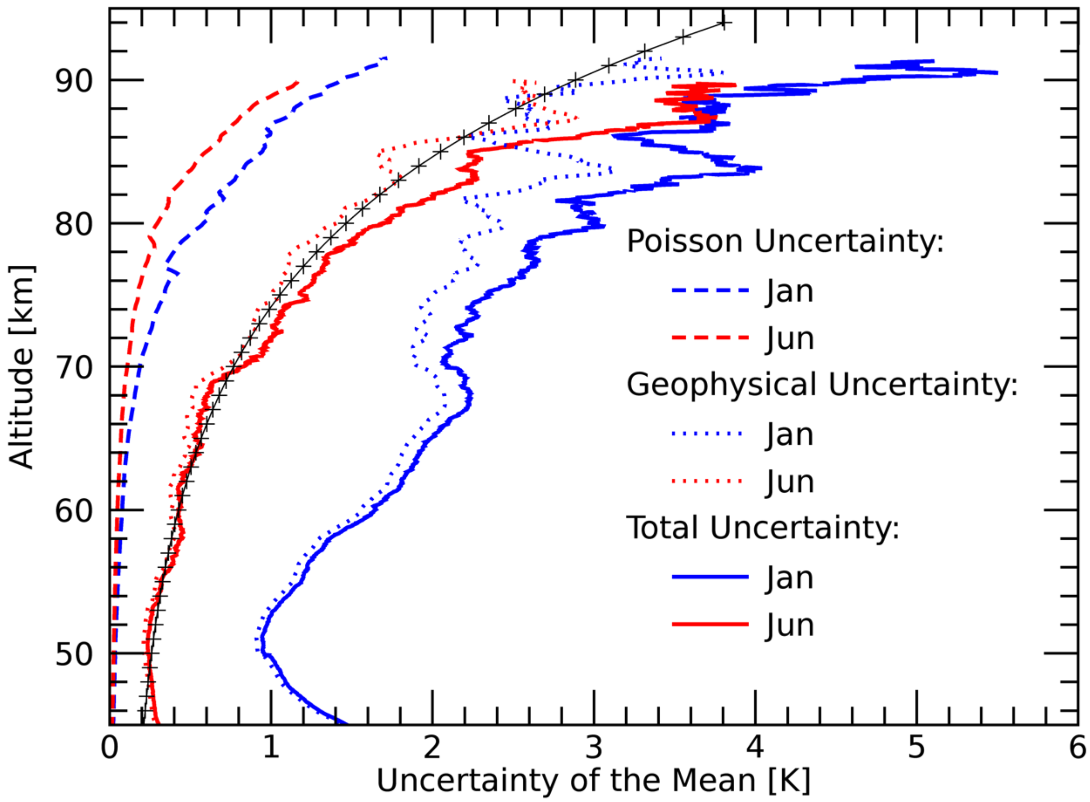

Figure 6. Several Uncertainty Profiles for January and June Climatological Temperatures. The dashed profiles are the uncertainty of the mean $\sigma_{\bar{T}}(h)$ derived from the Poisson, photon-counting uncertainty, Equation 2. The solid profiles are the standard deviations of the mean $s_{\bar{T}}(h)$ derived from the temperatures, Equation 4. The dotted profiles are the geophysical temperature variability of the mean $\sigma_{Geo}(h)/\sqrt{N}$ derived starting from Equation. 5. The January profiles are given in blue and the June profiles in red. The profile of plus signs is a reference curve for the June geophysical variability of the mean. It grows with a 14 km scale height.

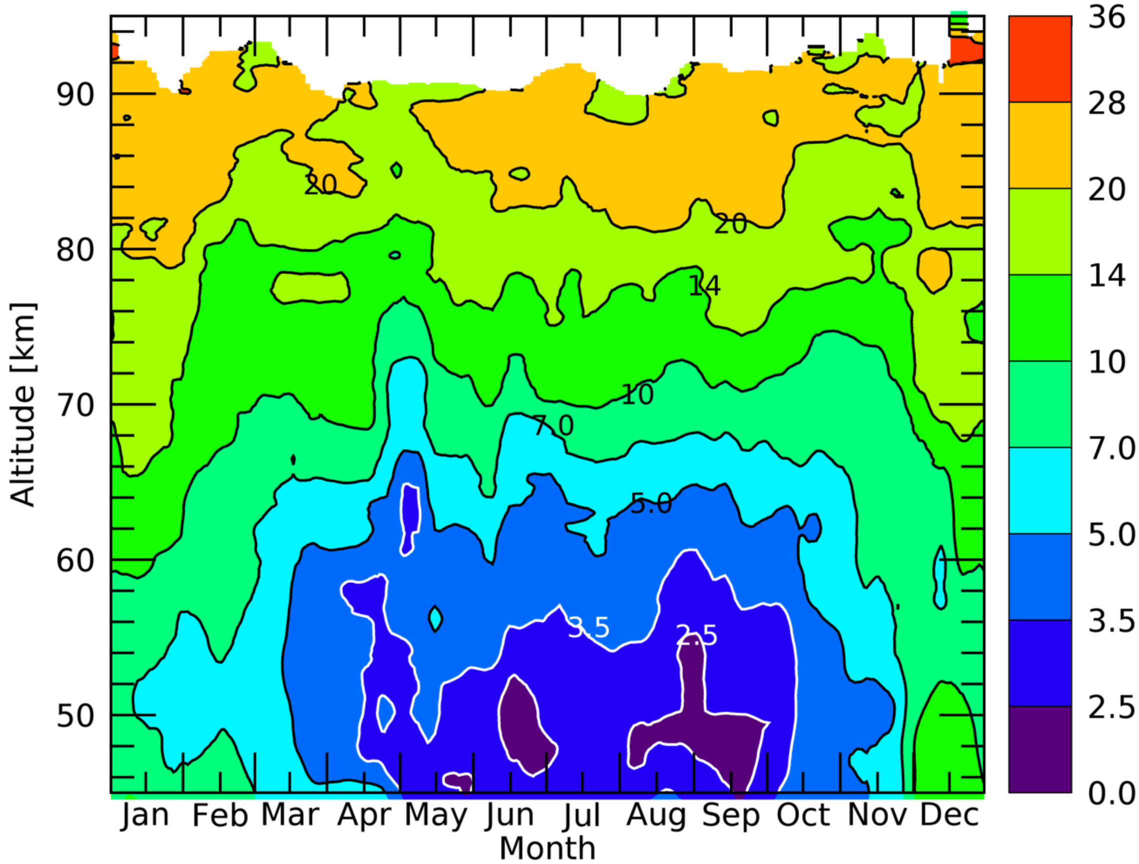

Figure 7. ALO-USU Composite Year Climatology of Geophysical Temperature Variability $\sigma_{Geo}(h)$. The variability $\sigma_{Geo}(h)$ is derived from the temperatures within the 31-day by 11-year window centered on each night of the composite year, Equation 5. The contours are at intervals increasing by $\sqrt{2}$ between 2.5 and 28 K.

Furthermore, $\sigma_{Geo}(h)$ can be divided by $\sqrt{N(h)}$, as done for other uncertainty expressions in Equations 2 and 4, to find the geophysical uncertainty of the mean of a particular set of $N(h)$ observations. This is what is shown by dotted lines in Figure 6 for January and June from the composite-year temperature variability.

3. Observations

3.1 Composite-Year Temperature Climatology

The average climatological temperatures can be examined in several ways. The temperatures for each day of the composite year are given as a contour plot in Figure 8 and are given at 3-km intervals in Table 1. This plot extends from 45 to approximately 90 km and from 175 to 270 K with contours every 5 K. For a second perspective and more detail, the averaged temperatures at three selected altitudes—45, 65, and 85 km—are shown in Figure 3. The three curves are very different, showing a singular characteristic of the mesosphere: the 45 km curve shows a cold winter and warm summer, while the 85 km curve shows the reverse, a warm winter and cold summer. There is a transition in between. After examining many curves between 60 and 70 km, the 65 km curve was chosen because it had the minimum variation. (It is purely coincidental that it is midway between 45 and 85 km.) The total uncertainty of the mean $s_{\bar{T}}(h)$, as defined in Equation 4, is also shown at monthly intervals on these three temperature curves. These uncertainties are all very small, giving considerable significance to the temporal structures in these curves and to the temperature values in the Figure 8 contour plot. For a third perspective and different detail, twelve altitude profiles of the monthly temperatures are shown in Figure 5. Each profile is the result of the same type of averaging as in Figures 3 and 8, the average of all the nighttime temperature profiles in a 31-day by 11-year window at each altitude $N(h)$.

However, in this case, the averages shown are just the` ones centered on the middle of each month. With so many profiles in Figure 5, it would be difficult and confusing to display the uncertainties, which are the total mean measurement uncertainties $s_{\bar{T}}(h)$ as also shown in Figure 3 at 45, 65, and 85 km. They are instead shown as profiles for each month in Figure 4. Again, they are small, small enough to enable meaningful comparisons among the temperature profiles in Figure 5. In addition to the monthly profiles, an annual average temperature profile, created by averaging the 12 one-month profiles, is shown in black. It almost perfectly divides the data in time, into summer and winter behaviors. (The exception is September above 78 km.) The monthly curves from the winter half of the year, October through March, are shown as dashed lines, and the curves from the summer half of the year, April through September, are shown as solid lines. Similarly, an annual average uncertainty profile is created and shown in black in Figure 4. Most of the uncertainty curves are closely clustered together. The biggest exception is December, which has the largest uncertainties. They reflect a combination of large, winter variability and the fewest number of nights observed.

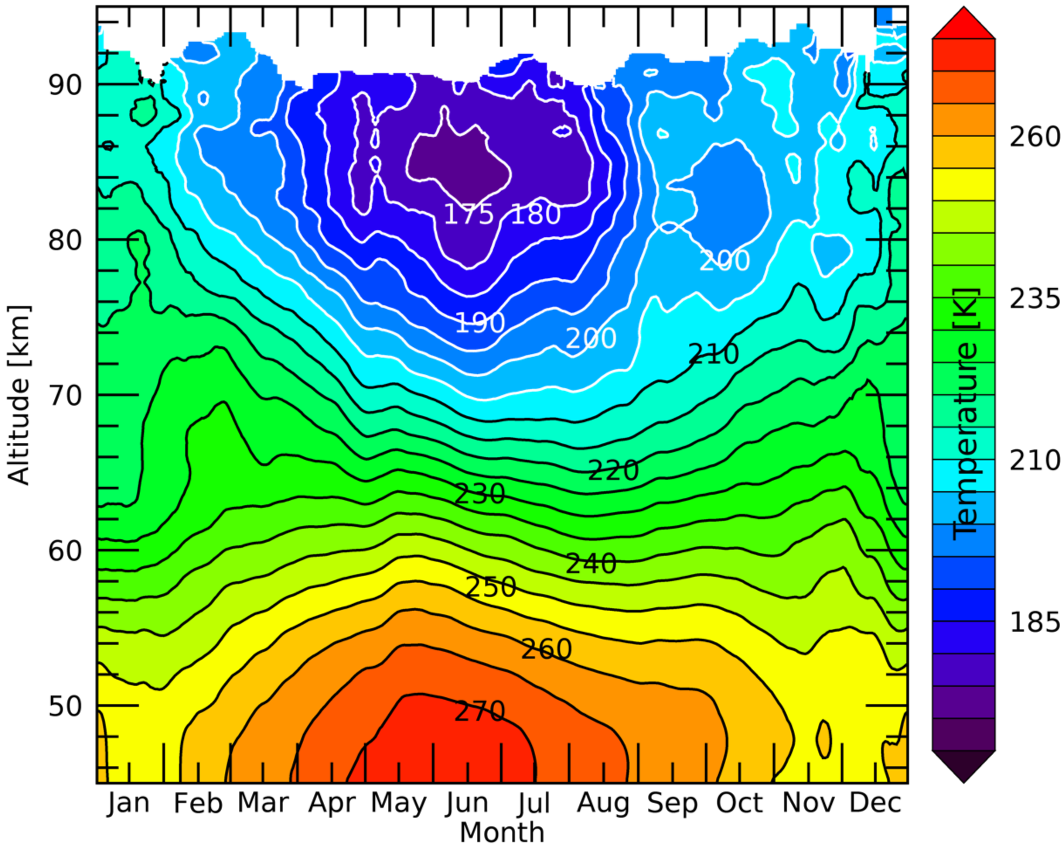

Figure 8. ALO-USU Composite Year Climatology of Nighttime Mesospheric Temperatures $\bar{T}(h)$ between 45 and ~90 km. The temperatures are averaged over a 31-day by 11-year window centered on each night of the composite year. The contours are at intervals of 5 K.

Table 1. Climatological Temperature Values and their Sample Standard Deviations of the Mean.

Alt	Jan	Feb	Mar	Apr	May	Jun	Jul	Aug	Sep	Oct	Nov	Dec
45	253.5	257.6	262.7	269.4	273.3	273.2	270.0	266.4	262.4	258.0	253.0	252.7
	1.5	1.2	0.6	0.8	0.4	0.3	0.3	0.4	0.3	0.5	0.8	2.6
48	253.2	256.2	262.1	266.9	271.7	272.1	269.2	265.6	262.6	259.3	254.4	254.5
	1.1	1.0	0.6	0.4	0.5	0.3	0.3	0.3	0.2	0.4	0.8	2.5
51	250.5	253.0	258.6	264.4	269.2	268.6	265.5	262.0	260.2	257.7	252.6	254.0
	1.0	0.9	0.6	0.5	0.5	0.2	0.3	0.3	0.3	0.4	0.7	2.2
54	246.3	248.0	253.9	259.8	264.8	262.9	259.2	255.8	255.3	253.5	249.1	251.4
	1.1	0.9	0.5	0.5	0.6	0.3	0.3	0.3	0.3	0.4	0.9	1.8
57	239.5	243.4	247.7	252.3	257.6	255.0	250.6	247.7	248.1	247.7	244.9	244.7
	1.3	1.1	0.5	0.5	0.7	0.4	0.4	0.4	0.3	0.5	1.0	1.4
60	231.9	237.5	240.9	244.5	248.6	245.1	240.7	237.4	239.2	240.5	241.3	238.8
	1.6	1.1	0.6	0.6	0.7	0.4	0.5	0.4	0.4	0.6	1.2	1.3
63	225.0	231.8	234.3	236.2	238.1	233.5	229.8	227.4	230.2	233.1	235.5	232.9
	1.9	1.1	0.7	0.7	0.7	0.5	0.5	0.5	0.5	0.6	1.2	1.4
66	222.7	231.0	229.3	229.0	227.4	220.6	218.7	217.3	220.8	226.3	228.8	229.4
	2.1	1.1	0.8	1.0	0.9	0.6	0.6	0.6	0.6	0.8	1.2	2.1
69	222.7	229.4	226.3	221.4	216.2	208.1	208.0	209.5	213.5	220.0	223.0	226.8
	2.2	1.3	0.9	1.4	1.2	0.7	0.8	0.9	0.8	0.9	1.3	2.8
72	222.7	225.5	220.7	213.6	206.5	197.7	201.5	203.5	208.0	214.0	218.2	222.9
	2.2	1.5	1.1	1.5	1.2	1.0	1.3	1.0	1.0	1.0	1.4	4.0
75	220.9	220.1	214.2	204.7	196.9	188.5	195.4	198.8	205.3	208.3	212.3	216.5
	2.3	1.5	1.3	1.5	1.6	1.2	1.3	1.2	1.4	1.2	2.0	3.5
78	218.2	215.0	206.3	195.6	190.3	179.7	188.6	193.7	202.4	203.2	208.2	210.2
	2.6	1.7	1.6	1.8	1.9	1.4	1.4	1.5	1.7	1.7	2.0	4.2
81	216.9	208.3	200.1	187.2	183.8	175.4	183.2	187.2	199.8	197.9	204.3	208.6
	2.9	2.0	1.8	2.0	2.0	1.8	1.8	2.0	1.9	1.8	1.8	4.0
84	212.9	203.7	196.7	183.1	176.7	171.2	177.3	183.9	200.6	198.0	203.7	209.4
	3.9	3.0	2.0	3.1	2.3	2.2	2.3	2.2	2.4	2.1	2.4	6.0
87	213.2	197.7	194.5	182.6	176.3	175.5	179.2	189.8	203.7	201.8	203.6	204.9
	3.8	3.1	2.4	2.7	2.9	3.5	2.5	3.2	2.8	2.4	3.7	6.1
90	211.8	202.1	195.7	186.4	180.5	—	180.8	—	197.2	201.6	201.1	208.6
	4.5	4.0	3.3	4.1	3.0	—	2.6	—	3.1	2.9	3.8	7.2
93	—	—	—	—	—	—	—	—	—	—	200.3	—
	—	—	—	—	—	—	—	—	—	—	4.4	—

Figure 2 shows the 48 individual nighttime temperature profiles for January and the 87 nighttime temperature profiles for June, which were averaged together, respectively, to make the January and June profiles in Figure 5. The averaged January and June profiles give rise to the extreme temperature profiles in Figure 5. Both months in Figure 2 show profiles of temperatures that mostly reflect geophysical variability and a small contribution derived from the Poisson contribution to the temperature uncertainty. Below ∼75 km the spread is clearly significantly greater in January than in June, presumably reflecting the propagation of more gravity waves and planetary waves into the mesosphere in winter (Andrews et al., 1987). In addition, in January, the distribution of curves appears to become wider below 50 km, presumably in response to SSWs (Sox et al., 2016). A few of the nights, roughly 10%, in both months clearly show profiles with large-scale waves with both bigger amplitudes and longer wavelengths than for the rest of the nights. The spread in the profiles increases with altitude. However, above ∼75 km the spread becomes very similar for the two months. Looking in detail at these collections of profiles, what is clear is the presence of waves with a wide range of vertical wavelengths and amplitudes that grow with altitude. The waves must have long enough periods and small enough vertical velocities that they show up strongly as waves in the all-night profiles. Above 92 km, the spread diminishes, not because of geophysical reasons, but because of the similarity of the initial temperature values, which are all taken from the CSU Na lidar climatology as stated earlier.

Most of the monthly profiles in Figure 5 start at a high temperature at 45 km and then decrease monotonically with altitude until the mesopause near 85 km. However, the profiles for January and February behave significantly differently from the others. At about 65 km, the temperatures start to increase with altitude. They do this for the next 5 to 10 km, then resume their monotonic decrease with altitude. That results in a small peak in the two profiles. In addition, the profiles for December and March change slope in this same region, briefly decreasing more slowly with altitude. This behavior, which is different than for the other eight months, comes about because of wintertime mesospheric inversion layers (Schmidlin, 1976; Hauchecorne et al., 1987; Whiteway et al., 1995, Leblanc and Hauchecorne, 1997; Meriwether and Gerrard, 2004). Examples of these inversion layers, one each from December, January, February, and March, are shown in Figure 9. These profiles were selected because they show very significant mesospheric inversion layers. By comparing them to the average profiles in Figure 5, note that they have temperatures below the average at ~65 km and above the average at ~75 km. However, the amplitude of mesospheric inversion layers does vary considerably from night-to-night as does their occurrence frequency. These variations in amplitude and occurrence frequency give rise to the differences seen in the averaged profiles in Figure 5.

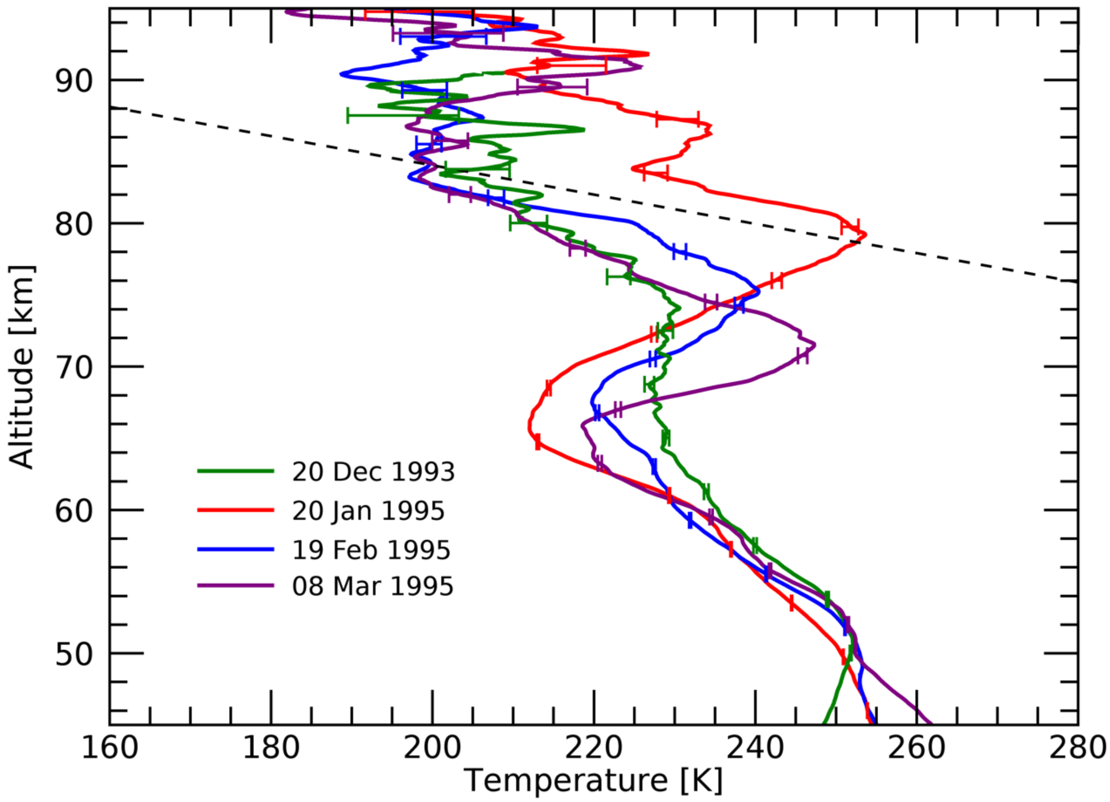

Figure 9. Temperature Profiles $T(h)$ from Four Winter Months with Large Mesospheric Inversion Layers. They are from 20 December 1993, 20 January 1995, 19 February 1995, and 8 March 1995. The error bars $\sigma_i(h)$ are calculated from the propagation of the Poisson uncertainty for the signal through the temperature reduction routine. The dashed line shows the adiabatic lapse rate. The January and February profiles have extensive regions on the topside of the inversion layer that are at the adiabatic lapse rate.

In Figure 9, these temperature profiles come from 20 December 1993, 20 January 1995, 19 February 1995, and 8 March 1995. Also, included for reference in Figure 9 is the adiabatic lapse rate of 9.8 K/km, which is extremely close to the topside lapse rate for two of these four all-night profiles. This closeness has been noted in a number of previous studies (e.g., Whiteway et al., 1995; Leblanc and Hauchecorne, 1997; Sica et al., 2007; Meriwether and Gerrard, 2004) and has been associated with wave saturation and convective instability. Also, shown for each all-night profile are several examples of the temperature uncertainties (or error bars) that are based on propagating the Poisson uncertainties from the observations though the temperature reduction procedures. It is very apparent that the inversion layer structures are very real.

3.2 Composite-Year Climatology of Geophysical Temperature Variability

An indication of the geophysical temperature variability is seen in the spread of the composite year temperature profiles from January and June in Figure 2. Formally, the spread in the temperatures at a given altitude is characterized by the variance $s_T^2(h)$ of all the temperatures about the mean at that altitude during the month, Equation 3. The sample temperature uncertainty or variability of the mean of those temperatures $s_{\bar{T}}(h)$ is given by Equation 4, which is plotted for January and June in Figure 6 as solid lines. The January curve shows greater uncertainty or variability of the mean than does the June curve. This is for two reasons in addition to greater geophysical variability: fewer observations, Figure 1; and lower densities, hence signals (Barton et al., 2016). This basic temperature uncertainty from the observations has two contributions. The first is the temperature uncertainty or variability $\sigma_T(h)$ arising from the observations, from the Poisson statistics of photon counting that are propagated through the data reduction to the temperatures. Its temperature uncertainty of the mean $\sigma_{\bar{T}}(h)$, given by Equation 2, is plotted for January and June in Figure 6 as dashed lines. It shows greater uncertainty of the mean for January than for June for the same reasons as above. There are fewer observations, Figure 1, and lower densities, hence signals (Barton et al., 2016). These temperature uncertainty values are much smaller than those for the total sample uncertainty of the mean. The second contribution, the major one, is the geophysical variability $\sigma_{Geo}(h)$, which arises from many possible geophysical sources, as described below. It gives the total contribution to the variability from these sources. It is found by subtracting the variance from Poisson statistics from the total sample variance, Equation 5. This is shown for the composite year in Figure 7 and the values given at 3-km intervals in Table 2. This result is then divided by $\sqrt{N(h)}$ to find the total geophysical variability or uncertainty of the mean, which is plotted for January and June in Figure 6 as dotted lines. It is only slightly smaller than the sample temperature uncertainty of the mean.

Table 2. Geophysical Temperature Variability σ_{Geo}.

Alt	Jan	Feb	Mar	Apr	May	Jun	Jul	Aug	Sep	Oct	Nov	Dec
45	9.9	8.7	4.9	6.1	2.6	2.8	3.2	3.5	2.5	4.3	5.0	12.5
48	7.3	7.2	5.2	3.2	3.6	2.4	2.7	2.5	2.2	3.9	5.0	12.3
51	6.6	6.8	5.0	3.5	3.9	2.2	2.7	2.8	2.6	3.7	4.6	10.7
54	7.6	7.2	4.3	3.6	4.5	2.8	3.0	3.0	2.7	3.8	5.7	8.8
57	8.9	8.2	4.7	3.4	5.1	3.9	3.8	3.5	3.2	4.7	6.3	6.7
60	11.4	8.8	5.2	4.3	4.9	4.1	4.6	3.9	3.7	5.2	7.4	6.3
63	13.0	8.8	6.0	5.0	5.3	4.7	4.9	4.6	4.4	5.3	7.5	7.0
66	14.5	8.9	7.2	7.5	6.6	5.3	6.6	5.9	5.5	7.1	7.8	10.2
69	15.3	10.6	8.8	10.3	8.9	6.2	8.4	8.6	7.5	8.6	8.1	13.7
72	15.5	11.9	10.3	11.6	8.8	9.3	13.6	10.3	10.3	9.4	8.7	19.4
75	16.3	11.9	12.2	11.5	11.6	11.3	13.6	12.2	14.1	10.8	12.4	17.3
78	17.9	13.4	14.7	13.2	13.4	13.3	14.3	14.9	16.6	15.9	12.4	20.5
81	19.9	15.4	16.3	14.0	14.5	16.7	17.9	20.0	18.2	16.5	11.1	18.8
84	25.9	22.1	17.4	20.8	15.7	20.2	21.9	21.2	23.2	19.1	14.9	25.2
87	22.5	22.0	19.8	17.0	18.6	27.3	24.0	27.1	25.2	20.8	21.4	24.4
90	24.0	25.2	23.4	21.0	15.9	—	21.4	—	23.4	21.3	19.9	24.8
93	—	—	—	—	—	—	—	—	—	—	19.2	—

As just mentioned, there are many potential sources of geophysical variability. These include waves with periods greater than half a night's observations that are not coherent with a 24-hr period, such as some gravity waves and planetary waves. Their contribution is apparent in Figure 2. Other sources include upward propagation of tropospheric temperature perturbations from weather systems, random sampling of episodic events such as time-varying mesospheric inversion layers or SSWs (and mesospheric coolings), solar variations from solar activity and the 27-day Carrington rotation, variability in the timing of the change from one season to the next, year-to-year variability from such things as El Niño and La Niña and the quasi-biennial oscillation (QBO), multi-year temperature heating or cooling from major volcanic eruptions such as El Chichon and Mt Pinatubo, solar cycle irradiance variations, and long-term temperature trends such as from global climate change. In addition, because of clouds affecting lidar observations, some of the observations include only the first half of the night and some only the second half of the night. As a result, there may also be some contribution to the variability from waves with a period roughly equal to the length of the night. Besides mesospheric inversion layers and SSWs, these sources of variation are not examined here. They will be in the future.

There is another possible contribution to the total uncertainty of the mean $s_{\bar{T}}(h)$ that needs to be mentioned. Because the data are averaged over 31-day periods, the total calculated uncertainty might be artificially increased if the temperature had a significant gradient in time. This possibility is explored by examining the effect of the largest temporal warming in the data, which occurred between early August and early September at 85 km, as shown in Figures 3 and 8. It is a 25 K temperature increase in the course of one month. Approximately 100 nights contributed to this portion of the composite climatology. An estimate of the effect of this temporal change is obtained by deriving the variance of the mean for a 25 K linear temperature change over this period. It works out to be less than 10% of the total variance, meaning that the effect on the total standard deviation of the mean is less than 0.2 K. Accordingly, the effect of temporal temperature gradients in the observations is small enough that it does not contribute significantly to these results.

Taken together these profiles of the January and June uncertainties of the mean in Figure 6 give a very good representation of the range of precision of the derived temperatures. The uncertainties shown in Figure 3 for 45, 65, and 85 km are the total uncertainties of the mean, calculated using Equation 4. The same is true for Figure 4. It should also be noted that these uncertainties are consistent with the temperature fluctuations in Figures 3 and 5. The values are small. They are less than 1.5 K below 70 km for the whole year except for December and January. They are that small, in part, because of the high photon count rates at low altitudes and, in part, because of the large number of nights observed each month, as indicated in Figure 1. They are bigger in December and January because of large winter wave effects and the smaller number of nights observed in December. They then have a rapid increase with altitude to values near 4 K by 90 km for most months and almost 8 K for December. This increase is largely because of the exponential falloff of neutral density with altitude. Another factor, as discussed in Section 2, is that the number of profiles contributing to the average at the maximum altitude $N(h_{max})$ is half of what it is at 45 km $N(45)$, with much of that decrease occurring in the top 10 km.

It should also be noted that the profile of the geophysical temperature variability of the mean for June in Figure 6 appears to increase exponentially with altitude over most of the altitude range. This is emphasized by a profile with plus signs almost superimposed on the June dotted curve. It grows by a factor of e every 14 km between 50 and 85 km. This is what is expected for waves growing adiabatically with altitude in an atmosphere where the density falls off with a 7-km scale height. This is presumably what is happening. The waves are growing at this rate as opposed to breaking and giving up energy, which would reduce the temperature variability.

Below 50 km something else is happening in Figure 6 in June. The variability grows above the background exponential level in descending from 50 to 45 km. This strongly suggests the existence of another source of temperature variability near the stratopause, a source that does not propagate upward. A possibility might be upward propagating gravity waves reaching their critical level and losing their energy to the background atmosphere.

The growth of the total geophysical variability of the mean $s_{\bar{T}}(h)$ in Figure 6 for January is less rapid and much more structured. Immediately above 86 km it has values similar to the elevated June values. Slightly lower, centered on 84 km, it has an isolated peak in variability. Below 70 km the variability is again significantly greater than what would be expected from a downward extension of an exponential profile. This additional variability must come from other geophysical processes. The relative maximum between 60 and 70 km most likely reflects the variability introduced by mesospheric inversion layers, such as the examples shown in Figure 9. Like the June profile, it also shows an increase while descending from 50 km to 45 km. However, this increase is significantly bigger. This is much like the temperatures in Figure 8 and at 45 km in Figure 3. This suggests another source of variability, which as mentioned earlier is most likely the intermittent occurrence of SSWs over the years during these observations (Sox et al., 2016).

The climatology of the geophysical variability for the composite year is given as a contour plot in Figure 7. As in Figure 8, this climatology is based on a 31-day by 11-year running average. This plot extends from 45 to approximately 90 km and from 2.5 to between 20 and 28 K with the contours increasing by $\sqrt{2}$. That is a meaningful spacing because, as already noted, the magnitude of fluctuations grows rapidly with altitude due to the exponential decrease in density, as described above. What is also immediately apparent in Figure 7, as suggested from Figure 6, is that in most of the mesosphere, there is considerably greater variability in December, January, and February than in summer. This winter variability grows and extends into the upper mesosphere above ~80 km. However, unlike the annual cycle in variability in the lower mesosphere, this high level of variability extends across almost all 12 months. In between the winter and summer periods of high variability, there are two short periods, each about a month long, with lower variability, less than 20 K instead of greater than 20 K. The first is centered on mid-April, three weeks after equinox. The second is centered on the beginning of November, five weeks after equinox. They do differ from one another in that the April period appears to extend lower into the middle and lower mesosphere than the November period. They both extend down to 70 km, with the spring one extending another 10 km or so lower. By their timing, they are related to the winter-summer seasonal transitions. With this high level of variability in both summer and winter, it appears that there is much greater variability above ~80 km in summer than expected from the variability below. This is supported by the high level of variability in the June profile in Figure 6 above 80 km, in the region of the mesopause.

In addition to June and January, the composite year contour plot in Figure 7 shows further variability in altitude and time, suggesting even more effects. It appears that from late May through October, the variability is similar to what is shown in Figure 6 for June. Strong winter effects occur from November well into February, and to a lesser extent into March. Variability in December is particularly strong at all altitudes. As indicated above, much of this may come from significant inversion layers.

The temperature variability distribution in the upper mesosphere above 80 km, as shown in Figure 7, is roughly the same throughout the year and quite large. However, a few aspects of it need mentioning. The winter period from early December through late March and the summer period from late May through early October have similar variability above about 80 km. The summer temperature variability starts at 14 K, increases to 20 K and in a few spots almost reaches 28 K. As mentioned above, this appears to be part of the exponential growth with a 14 km *e* folding distance. This might arise from the breaking of gravity waves at high altitudes or from variations in the meridional circulation. However, at the highest altitudes, above 88 km or so, the variability appears to decrease in Figures 2 and 7. This reflects that these altitudes are very close to where the initial value in the temperature data reduction is specified. Accordingly, the deduced variability at the highest altitudes would be artificially reduced. Coming back to just above 80 km, the higher-than-expected temperature variability may arise if the temperature profiles can vary significantly. That possibility is clearly seen in a few of the profiles with large amplitudes in Figure 2. It is further emphasized by the finding (Herron et al., 2007) of a wave on 22 June 1995 at 83 km that had a 20 K amplitude, which in that case gave rise to a low enough temperature to support a noctilucent cloud. To be clear, this high-temperature variability is a common feature during both the winter and summer periods. It extends across the March and September equinox periods as well as the very cold summer mesopause in June at 85 km. This indicates that no localized maximum in variability is seen at either equinox. As previously indicated, the temperature variability during the “cold island” in mid-October is smaller. This supports the contention that the “cold island” is a general feature, a true cold region in time and altitude, not the result of a few particularly cold nights.

Thus, from the lidar observations, temperatures have been obtained throughout the mesosphere between 45 and ~90 km during a composite year. Near 45 km, the summer is about 20 K hotter than the winter. Near 85 km, this behavior is reversed, with the summer mesopause about 40 K colder than the summer maximum. In spring, the periods of heating at 45 km and of cooling at 85 km are much shorter than the fall periods of cooling at 45 km and heating at 85 km. The transition between these two behaviors is at 65 km. In addition to this significant spring-fall asymmetry in temperature behavior, two features stand out. They are a period of extreme heating at 85 km of 25 K/month from early August to early September and a “cold island” that follows shortly thereafter in October. In winter, there is a “cold valley” extending from 45 km well into the middle mesosphere. There is considerable variability in the temperature profiles, which increases with altitude. There is a small contribution originating from the Poisson statistics of the observations and a much larger contribution from geophysical temperature variability. The two components combine to produce the observed variability. This variability is illustrated in Figure 2 and shown in Figure 6 for January and June. The composite-year climatology of the geophysical temperature variability is show in Figure 7.

4. Discussion

As discussed in the previous section, the ALO-USU mesospheric temperatures from 41.74° N latitude are presented in three different ways in Figures 3, 5, and 8: at three specific altitudes, as monthly profiles, and as contours. The geophysical variability is presented as a contour plot in Figure 7. The temperatures and variability from two other lidar groups located between 40° and 45° N latitude were presented as contours plots in their papers: the two French lidars, OHP at 44.0° N and 6.0° E and CEL at 44.0° N and 1.0° W (Hauchecorne et al., 1991;

Leblanc et al., 1998) and the Canadian Purple Crow Lidar (PCL) originally at 42.9° N and 81.4° W and now at 43.1° N and 81.3° W (Argall and Sica, 2007; Jalali et al., 2016). Although contour plots provide a good indication of how things vary with altitude and time, they do present a challenge for obtaining precise comparison values. There are additional considerations that affect these comparisons. While there is a significant overlap in altitude from 45 to 85 km, the individual lidars cover different ranges. The three groups handle the data, the photon counts, in slightly different ways and determine temperatures in slightly different ways. Both the altitude and temporal smoothing are done differently. In addition, the time periods covered by the reported observations are different: 1993 to 2004 for ALO-USU; 1984 to 1995 for OHP and 1986 to 1994 for CEL (Leblanc et al., 1998); 1994 to 2013 for PCL. The latter is further divided between 1994 to 2004 (Argall and Sica, 2007), which is used mostly for geophysical variability, and 1994 to 2013 (Jalali et al., 2016), which is used mostly for temperatures. Also, the seasonal coverage and density of observations differ: 839 nights at ALO-USU; 1244 profiles at OHP and 670 at CEL (Leblanc et al., 1998); and 453 profiles at PCL between 1994 and 2004 (Argall and Sica, 2007). Winter tends to present the greatest challenge because of both the observing conditions and the day-to-day or week-to-week variability of the temperatures. Another factor, the impact of which is not clear, is the proportion of the night that is observed—first half, second half, or all night. It could affect the precision as well as the contribution of tidal fluctuations to the “all-night” temperature averages and the geophysical variability.

Despite all these caveats and cautions, it is nonetheless very worthwhile to compare these two ALO-USU climatologies with those from the other two groups. There are many features that are common and others that are different. Because information from these other two groups will be referred to often, please note the references to Argall and Sica (2007) and Jalali et al

(2016) for PCL and to Leblanc et al (1998) for OHP and CEL and consider them as given whenever reference is made to these lidars or the results obtained with them.

4.1 Lower Mesosphere

In the lower mesosphere in summer, the maximum temperatures at ALO-USU occur in May and June, as seen in Figures 3, 5, and 8. If anything, May is comparable to or very slightly warmer than June. This result is similar to what is seen in the contours for the other lidars, especially OHP. For the others, there appears to be a slight maximum in June. The profiles for mid-May and mid-June in Figure 5 are at least 3 K warmer than any of the other profiles up to 52 km. This difference is valid in that it greatly exceeds the total observed uncertainty of the mean, given by the solid profiles in Figure 6 for June. These contours in Figure 8 also show time variations of temperature, i.e., heating and cooling rates, on both sides of the maximum. The heating rate in the spring is significantly greater than the cooling rate in the fall. The contours for the other lidars qualitatively show the same asymmetry, heating faster in the spring and cooling more slowly in the fall.

In winter, the mid-January temperature profile in Figure 5 is significantly colder than the December and February profiles, especially between 50 and 64 km, reaching more than 5 K colder near 58 km. Turning to the contours, they show very distinct temperature maxima on either side of this January minimum, creating a “cold valley” in between. In more detail, starting in late November, a relative maximum in Figure 8 appears to propagate upwards from about 55 km until mid-December at about 74 km. Then in mid-January a relative temperature maximum descends from 85 km until late February at about 65 km. The effect of these two warm features is to extend this “cold valley” beginning at about 75 km at the beginning of January and descending to about 50 km by the end of January. The center of this temperature minimum occurs between 1 and 5 weeks after winter solstice as it depends on altitude.

The winter behavior is complex and varied for all the lidars. There is more or less a minimum temperature between 45 and 50 km between November and February, but with one or two hot spots in between. All the lidars show significant increases in the geophysical variability between 45 and 50 km between December and February followed by decreases in variability between 50 and 60 km. The low altitude values rise to 10 K or so, compared to the summer values of 4 K or less from April to October. Like the hot spots, the dates of these minima vary somewhat within that period. ALO-USU and PCL have the coldest background temperatures, between 250 and 255 K, in this 45 to 50 km region. The two French lidars have slightly warmer background temperatures, between 255 and 260 K. ALO-USU has a hot region in excess of 255 K. PCL has two hot regions, one in excess of 255 K and one in excess of 260 K. OHP has a hot spot in excess of 260 K, while CEL has two hot spots, one in excess of 260 K and one in excess of 265 K. The variable timing of these hot spots on top of what are basically temperature minima strongly suggest that they arise from a non-radiative source. All groups have suggested that they could result from Sudden Stratospheric Warmings (SSWs). Major SSWs have been examined in detail at ALO-USU, i.e., at midlatitudes, between 1993 and 2004 by Sox et al. (2016). This SSW interpretation is consistent with what they found. Because of different observational periods, the hot spots would occur at different times between December and March. Because of averaging years with and without SSWs, the small 5 K temperature increases are reasonable. The extension of the hot spots to about 50 km is also consistent with this interpretation.

Turn from the variability between 45 and 50 km to the stratopause, which is located in or close to this region. The ALO-USU temperatures are shown in the composite temperature climatology in Figure 8 and the mid-month profiles in Figure 5. They vary between 253 and 273 K. As shown by the altitude of the relative maxima in the profiles, the stratopause is at approximately 47 or 48 km between July and January, but the lack of a clear relative maximum suggests it is at or below 45 km between February and June. This is similar to the other lidars. At PCL, the stratopause is above 45 km all year except for January and February. It is below 48 km except for December when it is just above 50 km, presumably because of SSW effects. At OHP and CEL, it is between 47 and 48 km most of the year, but drops to 46 km from December through February. Thus, all the mid-latitude lidars appear to show an annual cycle in the height of the stratopause with it being between 47 and 48 km most of the year, but dropping to close to or below 45 km between December and February. It appears to be just below 45 km at ALO and PCL and just above in France.

The curve for ALO-USU at 45 km in Figure 3 gives a good representation of the annual temperature cycle at that altitude. The maximum is 273.4±0.4 K in mid-May and the minimum is 250.3±1.2 K in late January, giving rise to a summer-winter difference of 23.1±1.3 K. As might be expected from the variability of SSWs, there is another relative temperature minimum of 252 K in early December with a small relative maximum of 257 K on 1 January in between these relative minima. With the exception of the SSW effects, there is a basic annual cycle of hot in summer and cold in winter. In more detail, while the temperature maximum is in mid-May, the temperature is almost the same throughout May and June, which implies that the maximum is approximately a month before summer solstice. While the minimum is in late January, the relative minimum in early December is almost the same. This suggests that the winter minimum is later than the winter solstice. In addition, the heating rate in spring and cooling rate in fall are at very different rates. Between the end of January and the end of April the temperature increases by almost 7 K per month. Between the end of June and the end of November the temperature decreases at about half that rate, 4 K per month. This asymmetry in the occurrence of the seasonal temperature extremes and the related asymmetry in the spring heating rates and fall cooling rates emphasizes the presence and contribution of physical processes that are more complicated than the annual variation of solar irradiance.

Along with the temperatures, the geophysical variability has distinctive patterns throughout the year. Looking at the region near 45 km, the variability is between 2.5 and 3.5 K from May through September. It then increases significantly to between 7 and 10 K between November and February. At PCL, the geophysical variability in the same summer period is between 2 and 4 K. It increases in winter, reaching 14 K in January. At the French lidars, it is between 3 and 4 K in the same summer period. It increases to 12 K in December and January. Thus, these mid-latitude lidars have essentially the same very small geophysical variability from May through September in the vicinity of 45 km. It increases in winter depending, most likely, on the occurrence of planetary waves and SSWs to values between 7 and 14 K primarily in December and January. However, the ALO-USU values are at the low end of that range.

4.2 Middle Mesosphere

A transition or crossover altitude between these different altitude regimes, with comparatively minimal seasonal variation, occurs at 65 km, as shown in Figure 3. However, there is still some temperature structure at this altitude, though it is mostly during the winter. It shows up as strong cooling during December from 233 to 221 K followed by slow recovery during January and February back to 232 K. This temperature decrease is the same for every such temperature curve that we have examined between 61 and 68 km. This behavior is also seen in the contour plot in Figure 8. It gives rise to what was earlier characterized as the “cold valley." The French lidars show bigger decreases, but during two months, from mid-November to mid-January. They are followed by comparable increases over the next two months. The pattern for the PCL lidar appears similar to the French pattern.

More generally, looking at the averaged temperature profiles in Figure 5 and inferred from Figure 8 is that the mesosphere, except for the upper-most part, is usually characterized by temperature profiles that decrease monotonically with increasing altitude. However, the great amount of averaging in January and February shows profiles in Figure 5 that become significantly more vertical (isothermal) or even increasing in a region just above 65 km. This more vertical structure also shows up in the superposition of individual nighttime profiles from January in Figure 2. In January, the average profile is almost isothermal between 64 and 74 km and in February between 63 and 68 km. In addition, the January temperature profile is almost 10 K colder than the February temperatures in the isothermal region, but then becomes as much as 15 K warmer above that region.

These changes in slope occur because the averaging includes many profiles with mesospheric inversion layers (Schmidlin, 1976; Hauchecorne et al., 1987; Whiteway et al., 1995, Leblanc and Hauchecorne, 1997, Meriwether and Gerrard, 2004) as well as many without. The inversion layers also have smaller but noticeable impacts on the December and March average profiles. The maximum effect of the inversion layers, in terms of increased temperature, occurs in January, a month after winter solstice.

To emphasize the point that these winter structures arise from inversion layers, examples of ALO-USU inversion layers from four individual nights from four separate months are shown in Figure 9. Below approximately the transition altitude, comparisons of the profiles in Figures 5 and 9 show that their temperatures below the inversions are significantly colder than the average profiles. At roughly the transition altitude, their temperatures increase sharply by 5, 10, or even 40 K, giving rise to a very distinct inversion layer peak 5 to 15 km higher. Above that peak, the temperatures decrease rapidly. Also, included in Figure 9 is a dashed line showing the adiabatic lapse rate of 9.8 K/km, which is the steepest gradient that can be sustained. If it were steeper, on the topside of the inversion layer, a convective instability would set in (Whiteway et al., 1995) that would return the gradient to the adiabatic lapse rate. Two of these all-night profiles show regions where the lapse rate is equal to the adiabatic lapse rate. These steep gradients, lasting all night, are a common feature of the ALO-USU mesospheric inversion layers. The low temperatures, compared to the average below 65 km followed by high temperatures at higher altitudes, suggest that the mesospheric inversion layers are a manifestation of a wave phenomenon, consistent with Meriwether and Gerrard (2004).

There is much less structure visible during the rest of the year. In particular, in the summer from May to August, there is a gradual temperature decrease at 65 km from 230 to 220 K. Furthermore, between 60 and 70 km, the temperature contours are essentially parallel and almost equally spaced. This summer region has the biggest temperature gradient, falling approximately 4 K/km with increasing altitude. The PCL and the French lidars show similar smooth temperature contours and large temperature gradients in this region.

This part of the year roughly coincides with low geophysical temperature variability. However, the low variability starts one to two months earlier in the spring and extends one to two months later in the fall than the region of almost parallel, gradually decreasing temperatures. During this period, the variability ranges from 5 K near 60 km to 10 K near 70 km. The behavior is similar at PCL and the French lidars except that their maximum variability is smaller. The values at PCL are roughly between 4 and 6 K. The combined values for the French lidars are between 4 and 7 K. In the winter months from November through February, it increases to between 10 and 14 at ALO-USU. It reaches 14 to 18 K at PCL in late December and early January and 13 to 14 at the French lidars in late December.

4.3 Upper Mesosphere and Mesopause

In the upper mesosphere in Figures 5 and 8, and at 85 km in Figure 3, the phasing of the seasonal behavior is reversed from that of the lower mesosphere, with a warm winter and a cold summer. This well-known behavior reversal is also seen for the French lidars and the Canadian lidar. The lowest temperature in the ALO-USU data is a minimum of 169.8±2.3 K in early June at 85 km, which is closer to summer solstice than the center of the extended summer temperature maximum at 45 km. The June profile in Figure 5 is colder than any other profile above 70 km, becoming 7 to 10 K colder than the May and July profiles above 75 km. As mentioned above, it has a distinct minimum at 85 km, which is the summer mesopause. This behavior is in close agreement to what was found with the PCL. In their case, the downward integration started some 10 to 15 km higher, making their results essentially independent of the initial value. Unfortunately, the French lidars do not have results for the region above 85 km. This summer mesopause behavior is also in close agreement with the findings obtained with Na lidar, e.g., at CSU (40.6° N, 105.0° W; She and von Zahn, 1998).

In the averaged profiles and the contour plot, this summer mesopause at ALO-USU extends from April to August with altitudes that are within 1 to 2 km of the June 85 km altitude and the temperatures rising approximately 15 K on either side of June. Beyond these extremes, March appears to have a minimum that is 3 km higher and 12 K warmer than June. September has a minimum of 200 K, which is 30 K warmer than June, that appears to be 3 km lower than the June minimum. And, very unusually, September has a relative maximum at almost 87 km.

This is from the very rapid heating described earlier that extends from August into September. However, this lower altitude September minimum may be part of another phenomenon, a “cold peninsular,” which is seen by the other Rayleigh lidars extending to lower altitudes. However, at ALO-USU it leads to a “cold island,” which is discussed below. The mesopause is so cold in these summer months and March that the average of all the monthly profiles in Figure 5 also shows a mesopause at 85 km. These mesopause results are similar to those reported for the PCL. Their mesopause extends from April through September. It is at 87 km in June and within 1 km of that in the other months.

In addition to the mesopause, another temperature minimum, a 5 K relative minimum, occurs at ALO-USU just before mid-October. It is centered at 82 km and extends from 78 to 86 km. It appears clearly in Figure 8 and shows up in Figures 3 and 5. It is 197 K at its coldest. The defining contour is at 200 K. This is the “cold island” referred to above. Since no unusual variability stands out in the geophysical temperature variability in Figure 7, it is probably a general feature. These observations are also most likely related to ones reported for PCL and the French lidars. Instead of a “cold island,” they observed a “cold peninsula” extending downward from the summer cold region in September into October near 80 km. The defining contours are in October at 195 K and 200 K for PCL and 210 K for OHP and CEL. Having been observed by four lidars, this “cold island” or “cold peninsula” is most probably a real feature that needs to be understood.

Unfortunately, these Rayleigh observations do not go high enough to investigate the winter mesopause.

Another distinctive feature appears at and near 85 km just before the “cold island” or “cold peninsula.” The summer cold region ends abruptly at ALO-USU with a very sharp one-month temperature increase of 25 K/month (about 4 times the usual) from early August to early September. This is a dramatic part of the asymmetry between the spring cooling rate and the fall warming rate. The fast, month-long heating is also seen by at least one of the French lidars, but surprisingly not by PCL. They have slower temperature increase over a longer period. It is followed immediately at ALO-USU by the cooling that leads to the October "cold island."

In mid-winter in the upper mesosphere (at 85 km in Figures 3, 5, and 8) the maximum temperature is 215.0±4.0 K on 31 December, shortly after winter solstice. In addition, the January profile stands out as it is significantly warmer than any other profile above 75 km, reaching more than 10 K warmer at several altitudes. As already indicated, the summer minimum at 85 km is 169.8±2.3 K in early June. These winter-summer temperature extremes give rise to a 45.2±4.7 K seasonal difference, which is essentially double the summer-winter extremes at 45 km and, of course, out of phase with it. This temperature behavior in the upper mesosphere is consistent with control by dynamics. It is usually attributed to the effect of planetary waves and, in particular, gravity waves on the global meridional circulation. These lead to adiabatic heating from downward compression in the winter hemisphere and adiabatic cooling from upward expansion in the summer hemisphere (Andrews et al., 1987; Holton and Alexander, 2000). Presumably the cooling from January to June, the slower heating from June through December, and the fast heating in August reflect details of this interhemispheric circulation.

At 85 km in the five months between January and June there is rapid cooling, averaging 9 K/month, but reaching values closer to 19 K/month for brief periods at the beginning of February and April. Initially, the winter geophysical temperature variability is high, greater than 20 K, presumably because of day-to-day and year-to-year differences. In March and April, while the temperature is still falling, this variability drops below 20 K. It then increases leading up to the June temperature minimum and continues high throughout the summer and early fall. Meanwhile, the temperature increases, overall averaging just under 7 K/month between early June and the end of December. However, as already mentioned, it has significant structure superimposed on that rate between mid-July and early October. Initially, there is a brief period of slow cooling between mid-July and early August. That is followed by a very striking period of rapid heating, approaching 25 K/month, for one month between early August and early September. This heating is followed by another brief period of slow cooling between early September and early October leading up to the October "cold island." The heating then becomes structured, but is on average just under 7 K/month until the end of the year. The summer temperature variability remains just above 20 K even during the very rapid temperature increase in August. It then drops below 20 K at the "cold island" in October and stays low until the beginning of winter in December at which point it increases to above 20 K again.

The PCL and the French lidars show much the same temperature pattern. There is the period of significant cooling from January to mid-June followed by a period of slightly slower heating until the end of the year. Superimposed on this, they all have a period of more rapid heating in August just prior to the "cold peninsula." The French lidars have rapid heating similar to ALO-USU in August, while the heating for PCL is less rapid.

In a significant difference from lower in the mesosphere, the geophysical temperature variability is greater for ALO-USU in the upper mesosphere than for the other lidars. With the exception of two, small time periods described above, it is between 14 and 20 K at 80 km over most of the year. At 85 km, it is between 20 and 28 K for most of the year. For PCL, with the exception, again, of two small, time periods, the values are between 6 and 10 K for most of the year at 80 km. It is the same for 85 km, except in January, when some of the seasonal variation appears, and it rises to 12 K. For OHP and CEL, the geophysical temperature variability retains a seasonal variation during the year. It too is much lower, from 9 to 10 K at 80 km from March through October, and increases to between 11 and 12 K at 85 km. It rises to 15 K at both altitudes in winter.

Provided the calculations are truly the same for each lidar, the greater geophysical temperature variability at ALO-USU implies less energy loss from upward propagating waves or additional sources of variability. It is not clear why the loss would be less or what other sources of variability would become significant.

4.4 Whole Mesosphere

Combining these summer and winter temperature results, the seasonal transitions are temporally asymmetrical, with slightly different asymmetry in the lower and upper mesospheres. In the lower mesosphere, as seen most clearly in Figure 3, the transition from midwinter (end of January) to midsummer (early May) takes three months while the transition from midsummer (early July) to midwinter (early December) takes approximately five months. In the upper mesosphere, the transition from midwinter (mid-January) to midsummer (early June) takes approximately five months while the transition from midsummer (early June) to midwinter (early January) takes approximately seven months. In both regions, the spring change is much shorter than the fall change. The source of this asymmetry is not apparent. However, this asymmetry would lead to the presence of a strong semiannual and probably higher-order temperature variations. These higher-order variations and their phases have been shown elsewhere for ALO-USU (Herron, 2007; Wynn, 2010).

This division between the lower and upper mesosphere that is based on temperature behavior does not extend to everything. Many gravity waves pass from the lower to the upper mesosphere at ALO-USU (Kafle, 2009). Many waves, both small scale and large scale, are seen in Figure 2 growing in amplitude as they propagate into the upper mesosphere. In addition, some temperature structures extend from the lower to the upper mesosphere. For instance, a large feature of warm air appears to propagate upward from 55 km in late November to 85 km in mid-January, contributing to the winter temperature maximum in the upper mesosphere. It then appears to propagate back downward to 65 km in mid-February. The region that lies between these two elevated temperature structures forms the January "cold valley," which appears to be closely related to the mesospheric inversion layers.

5. Summary and Conclusions

We have presented mid-latitude composite climatologies of nighttime mesospheric temperatures and of their geophysical variability derived from Rayleigh-scatter lidar observations at ALO-USU between 1993 and 2004. With over 5273 hours of data from over 839 nights analyzed out of 5972 hours and 964 nights acquired over a span of 11 years, this dense dataset is significant for investigating the vertical and temporal structure of the mesosphere. The lidar was described in Section 2. The observations were presented in Section 3. They were discussed and compared to observations from lidars at similar latitudes, from PCL in Canada and from OHP and CEL in France, in Section 4.

Overall, the temperature climatology shows the well-known features of the low-altitude mesosphere being hot is summer and cold in winter, while the high-altitude mesosphere is hot in winter and cold in summer. More specifically, at 45 km the temperature varies over 23 K, from 250 K in very late January to 273 in mid-May. At 85 km the temperature varies over 45 K, from

215 K at the end of December to 170 K at the mesopause in early June. The transition altitude between these opposite behaviors is 65 km.

While the solar irradiation follows a symmetrical increase and decrease during the year from winter-to-summer solstices, the temperature variations are decidedly asymmetrical, with a shorter period of change in the spring than in the fall. At 45 km, the temperatures increase in the spring at 7 K/month between the beginning of February and the beginning of May. In the fall they decrease at 4 K/month from the beginning of July to the middle of November. At 85 km, they decrease in the spring at 9 K/month from mid-January to early June. In the fall they increase at 6 K/month between early June and the end of December. Accordingly, the annual temperature variation needs to include semiannual and higher-order terms to describe the asymmetrical variation. The physical causes for this asymmetry need to be identified and examined. For instance, what are the roles of local and global dynamics in this asymmetry?

In the lower mesosphere, the stratopause is visible during part of the year. It is at ∼48 km from July to January with temperatures dropping from 270 to 252 K. It is at or below 45 km during the rest of the year.

In the upper mesosphere, the mesopause occurs in early June at 85 km at 169.8±2.3 K in heavily averaged data. (It has to be averaged because of the presence of waves.) The mesopause appears at slightly higher altitudes and at higher temperatures starting as early as March. It appears at slightly lower altitudes and higher temperatures in September. At the two extremes, the temperatures are 25-to-30 K warmer. From March to September, this summer mesopause is so pronounced that it shows up at 85 km in the annual average temperature profile.

A couple of features stand out at and near 85 km. A very sharp one-month temperature increase of 25 K/month (about 4 times the usual) occurs between early August and early

September. This is part of the asymmetry between the spring cooling rate and the fall warming rate. It is also seen by the French lidars (Leblanc et al., 1998), but surprisingly not as strongly by PCL (Argall and Sica, 2007; Jalali et al., 2016). It is followed immediately by a cooling, leading to an October "cold island," extending from 78 to 86 km that is ∼5 K cooler than the surroundings. The small geophysical variability during this period indicates that it is a general feature. The reality of this feature is further supported by a "cold peninsula," as opposed to an island, seen with the other lidars extending from the summer cold region down into the October location of the "cold island." These are clearly real features that need to be understood.

As expected, the geophysical temperature variability is much greater in the upper mesosphere than in the lower mesosphere. In June, it increases exponentially over most of the altitude range with, roughly, a 14 km *e* folding distance. It approximates this rate in other summer months. This growth rate suggests that the variability is largely from the adiabatic growth of waves with altitude. The waves have a wide range of wavelengths and amplitudes. This variability in summer in the upper mesosphere at ALO-USU is greater than what the other lidars show. It is close to 20 K, approximately 50% bigger than at PCL (Argall and Sica, 2007). This high level of variability in summer leads to a roughly constant level of variability throughout the year. This constancy is similar to PCL (Argall and Sica, 2007), but at a higher level. It is very different from the French lidars, which retain their annual variability with a winter maximum (Leblanc et al., 1998).

One aspect of these growing waves in summer is that waves at 85 km with a 20 K amplitude can and do exist. They can lower the temperature to 150 K, low enough to support a noctilucent cloud (Herron et al., 2007). While this low temperature happens often enough in June, the fact that few NLCs are seen indicates that it takes more than a low temperature to produce a noctilucent cloud. It could be a change in another parameter, such as water vapor, that enabled the NLCs to form above ALO-USU.

Departures in the geophysical variability from this growth rate curve with its 14 km *e* folding distance can be indicators of other various geophysical effects. For instance, the variability is greater than this curve between 45 and 50 km in the January profile and in the contour plot in December and January. This is presumably because of the intermittent occurrence of SSWs (Sox et al., 2016). It appears to be greater above 80 km during this same winter time period, which may indicate the mesospheric coolings are part of the intermittent SSW phenomenon. The variability is greater than this curve between 45 and 50 km in June. This might represent the effects of ascending waves being absorbed at their critical levels. The variability is also greater than this curve in winter between 60 and 70 km. This is presumably because of the intermittent occurrence of mesospheric inversion layers, which are significant enough to affect the month-long average profiles between December and March. They have two effects. On the bottom side of the inversions, they lead to colder-than-average temperatures, creating a “cold valley” centered on January, but extending from December to February at 50 to 70 km. It is most dramatic between 60 and 70 km in December and January. On the top side of the inversion, they lead to higher-than-average temperatures nominally between 65 and 75 km. Four examples of inversion layers are given. Their all-night profiles show a topside lapse rate very close to or equal to the adiabatic lapse rate, which is an indication of wave saturation and convective instability. The inversion layers, with a lower-than-average temperature below the maximum temperature and a greater-than-average temperature above the maximum temperature, suggest an amplified wave.

Temperature variability above 80 km lacks the winter-summer differences seen at lower altitudes. This appears to result from extra variability in the summer months between May and September. This might result from the waves ascending into this region without breaking. Alternatively, this might result from variability in the summer northward meridional flow. There are month-long periods with reduced variability starting shortly after the spring and fall equinoxes, one centered on mid-April, the other on early November. Given the timing, shortly after the equinoxes, might these two periods of reduced variability be related to a slightly delayed reversal in the interhemispheric circulation?

In addition to temperatures and variability, this extensive dataset has been used to investigate a number of aspects of the middle atmosphere such as SSWs (Sox et al., 2016), gravity waves (Kafle, 2009), neutral densities (Barton et al., 2016) and special events such as noctilucent clouds (Wickwar et al., 2002; Herron et al., 2007). Initial efforts have also been made to examine the combined effects of solar variations and climate change on the observed temperatures (Wynn, 2010).

While much has been learned from this extended mesospheric dataset from ALO-USU, still more can be learned from it. To further explore the mid-latitude mesosphere, more extensive comparisons are needed with other Rayleigh lidars located between 40° and 45° N, and with both empirical and reanalysis atmospheric models and with first-principle models. To explore the mesosphere more globally, comparisons are needed with Rayleigh lidars at both lower and higher latitudes.

A number of additional questions can be examined with new and improved data. The ALO-USU data set is just long enough to give an inkling about long-term trends (Wynn, 2010). However, the atmospheric system is variable enough that systematic longer-term observations are needed to properly separate long-term trends from short-term variations. Frequent observations are also needed to examine structures and trends in such features at the stratopause and mesopause, as well as to capture and examine special or unusual events. The SSWs and noctilucent clouds are examples. They were unexpected at a midlatitude site when lidar operations began, but their observations have furthered what we know about them. Additional observations of NLCs and correlative observations are needed to better understand their appearance.

Extended observations are needed from a more sensitive Rayleigh-lidar system, such as the one that has already been built and tested at ALO-USU (Wickwar et al., 2016; Sox et al., 2017), that is on the threshold of reaching 120 km. It improves the temperatures in the upper mesosphere and extends the observations upward well into the lower thermosphere. Downward extensions of the lidar observations are also needed to better relate mesospheric and thermospheric temperatures and their variability to what is happening in the stratosphere and troposphere. Continued observations, adding to what has been observed in the last 20 to 30 years, will help in determining the climatological changes.

Acknowledgments and Data

This work was supported in part by Utah State University, NSF Grants ATM-9203034, ATM-9302118, ATM-9714789, ATM-0123145, and ATM-0531397, a scholarship from the Rocky Mountain NASA Space Consortium, and personal resources. The lidar observations were carried out by a dedicated group of students: Brian Anderson, Allyson Bares, Angela Bodrero Beecher, Kayla Brown, Nathan Bunderson, Courtney Butler, Casey Clegg, Steve Collins, Joel Drake, Scott Elkington, Will Fredin, Spencer Fuller, Joshua Herron, John James, Teresa Jones, Jeffrey Leek, Eric Lundell, Bethany Martineau, Dusty McEwen, Ian Monson, Patrick Neary, Karen Marchant Nelson, Spencer Nelson, Antony Pearson, Robert Ream, Ryan Smith, Joseph Andy Spencer, Kristina Thomas, Ashley Turner, Marie Westbrook, and Troy Wynn. We thank John W. Meriwether of Clemson University and Thomas D. Wilkerson of the University of Maryland and then of Utah State University for contributing some of the components comprising the lidar system. We also thank John W. Meriwether, Xing Gao, Scott Elkington, and Kenneth C. Beissner for early contributions to the temperature data reduction, Ian Monson and Steve C. Collins for significant contributions to setting up the lidar system, and John Maloney for many nights of observing before the students became involved. We acknowledge several good exchanges with Robert Sica and Steve Argall of the University of Western Ontario concerning the temperature data reduction.

The Rayleigh lidar data for this study are available at https://digitalcommons.usu.edu/all_datasets/XXX/.

References

Andrews, D. G., Holton, J. R., & Leovy, C. B. (1987). *Middle atmosphere dynamics*. (No. 40). San Diego, CA: Academic.

Argall, P. S., & Sica, R. J. (2007). A comparison of Rayleigh and Sodium Lidar Temperature Climatologies, *Annales Geophysicae*, *25*, 27–35. https://doi:10.5194/angeo-25-27-2007

Barton, D. L., Wickwar, V. B., Herron, J. P., Sox, L., & Navarro, L. A. (2016). Variations in mesospheric neutral densities derived from Rayleigh lidar observations at Utah State University, *EPJ Web of Conferences*, *119*, 13006. https://doi:10.1051/epjconf/201611913006

Beissner, K. C. (1997). Studies of mid-latitude mesospheric temperature variability and its relationship to gravity waves, tides, and planetary waves, (Doctoral Dissertation), Retrieved from (http://digitalcommons.usu.edu/etd/4687). Logan, UT: Utah State University.

Gardner, C. S. (1989), Sodium resonance fluorescence lidar applications in atmospheric science and astronomy, *Proeedings of the IEEE*, *77*(3), 408-418. https://doi:10.1109/5.24127

Gerding, M., Höffner, J., Lautenbach, J., Rauthe, M., & Lübken, F.-J. (2008), Seasonal variation of nocturnal temperatures between 1 and 105 km altitude at 54° N observed by lidar, *Atmospheric Chemistry and Physics*, *8*, 7465-7482. https://doi:10.5194/acp-8-7465-2008

Goody, R. M., & Yung, Y. L. (1989), Atmospheric Radiation (Theoretical Basis), 2nd ed, New York, NY: Oxford.

Hauchecorne, A., & Chanin, M. L. (1980), Density and temperature profiles obtained by lidar between 35 and 70 km, *Geophysical Research Lett*ers, *7*, 565-568. https://doi:10.1029/GL007i008p00565

Hauchecorne, A., Chanin, M.-L. & Keckhut, P. (1991), Climatology and trends of the middle atmospheric temperature (33–87 km) as seen by Rayleigh lidar over the south of France, *Journal of Geophysical Research*, *96*(D8), 15297–15309. https://doi:10.1029/91JD01213

Hauchecorne, A., Chanin, M. L. & Wilson, R. (1987), Mesospheric temperature inversion and gravity wave breaking, *Geophysical Research Lett*ers, *14*(9), 933-936. https://doi:10.1029/GL014i009p00933

Herron, J. P. (2004), Mesospheric Temperature Climatology Above Utah State University, (Master's thesis). Retrieved from (http://digitalcommons.usu.edu/etd_physics/1). Logan, UT: Utah State University.

Herron, J. P. (2007), Rayleigh-scatter lidar observations at USU's Atmospheric Lidar Observatory (Logan, UT) — Temperature climatology, temperature comparisons with MSIS, and noctilucent clouds, (Doctoral dissertation). Retrieved from (http://digitalcommons.usu.edu/etd/4686). Logan, UT: Utah State University.

Herron, J. P., Wickwar, V. B., Espy, P. J., & Meriwether, J. W. (2007), Observations of a noctilucent cloud above Logan, Utah (41.7°N, 111.8°W) in 1995, *Journal of Geophysical Research*, *112*, D19203. https://doi:10.1029/2006JD007158

Holton, J. R., & Alexander, M. J. (2000), The role of waves in the transport circulation of the middle atmosphere, in Atmospheric Science across the Stratopause. In D. E Siskind, S. D. Eckermann, M. E. Summers (Eds.), *Geophysical Monograph Series* (Vol. 123, pp. 21-35). Washington, DC: American Geophysical Union. https://doi:10.1029/GM123p0021

Jalali, A, Sica, R. J.,& Argall, P. S. (2016), Extending and merging the Purple Crow Lidar temperature climatologies using the inversion method, *EPJ Web of Conferences*, *119*, 17005. https://doi:10.1051/epjconf/201611917005

Kafle, D. N. (2009), Rayleigh-lidar observations of mesospheric gravity wave activity above

Logan, Utah, (Doctoral Dissertation). Retrieved from (http://digitalcommons.usu.edu/etd/466). Logan, UT: Utah State University.

Keckhut, P., Hauchecorne, A., & Chanin, M.-L. (1993), A critical review of the database acquired for the long-term surveillance of the middle atmosphere by the French Rayleigh lidars, *Journal of Atmospheric and Oceanic Technology*, *10*, 850–867. https://doi:10.1175/1520-0426(1993)010<0850:ACROTD>2.0.CO;2

Leblanc, T., & Hauchecorne, A. (1997), Recent observations of mesospheric temperature inversions, *Journal of Geophysical Research*, *102*, 19471–19482. https://doi:10.1029/97JD01445

Leblanc, T., McDermid, I. S., Keckhut, P., Hauchecorne, A., She, C.-Y., & Krueger, D. A. (1998), Temperature climatology of the middle atmosphere from long-term lidar measurements at middle and low latitudes, *Journal of Geophysical Research*, *103*(D14), 17191-17204. https://doi:10.1029/98JD01347

Meriwether, J. W., & Gerrard, A. J. (2004), Mesospheric inversion layers and stratospheric temperature enhancements, *Reviews of Geophysics*, *42*, RG3003. https://doi:10.1029/2003RG000133

NIMA (2000), Department of Defense World Geodetic System 1984 — Its definition and relationships with local geodetic systems, National Imagery and Mapping Agency, Bethesda, MD.

Picone, J. M., Hedin, A. E., Drob, D. P., & Aikin, A. C. (2002), NRLMSISE-00 empirical model of the atmosphere: Statistical comparisons and scientific issues, *Journal of Geophysical Research*, *107*(A12), 1468. https://doi:10.1029/2002JA009430

Schmidlin, F. J. (1976), Temperature inversions near 75 km, *Geophysical Research Letters*, *3*(3), 173-176. https://doi:10.1029/GL003i003p00173

She, C. Y., & von Zahn, U. (1998), The concept of two-level mesopause: Support through new lidar observation, *Journal of Geophysical Research*, *103*, 5855-5863. https://doi:10.1029/97JD03450

She, C. Y., Chen, S., Hu, Z., Sherman, J., Vance, J. D., Vasoli, V., White, M. A., Yu, J. R., & Krueger, D. A. (2000), Eight-year climatology of nocturnal temperature and sodium density in the mesopause region (80 to 105 km) over Fort Collins, CO (41°N, 105°W), *Geophysical Research Lett*ers, *27*, 3289-3292. https://doi:10.1029/2000GL003825

Sica, R. J., Zylawy, Z., & Argall, P. S. (2001), Ozone Corrections for Rayleigh-Scatter Temperature Determinations in the Middle Atmosphere, *Journal of Atmospheric and Oceanic Technology*, *18*, 1223–1228. https://doi:10.1175/1520-0426(2001)018<1223:OCFRST>2.0.CO;2

Sica, R. J., Argall, P. S., Shepherd, T. G., & Koshyk, J. N. (2007), Model-measurement comparison of mesospheric temperature inversions, and a simple theory for their occurrence, *Geophysical Research Letters*, 34(23), L23806. https://doi:10.1029/2007GL030627

Sica, R. J., Sargoytchev, S., Argall, P. S., Borra, E. F., Girard, L., Sparrow, C. T., & Flatt, S. (1995), Lidar measurements taken with a large-aperture liquid mirror. 1. Rayleigh-scatter system, *Applied Optics*, *34*(30), 6925–6936**.** https://doi:10.1364/AO.34.006925

Sox, L., Wickwar, V. B., Fish, C. S., & Herron, J. P. (2016), Connection between the midlatitude mesosphere and sudden stratospheric warmings as measured by Rayleigh-scatter lidar, *Journal of Geophysical Research Atmospheres*, *121*, 4627-4636. https://doi:10.1002/2015JD024374

Sox, L., Wickwar, V. B., Yuan, T., & Criddle, N. (2017), Simultaneous Rayleigh-Scatter and

Sodium Resonance Lidar Temperature Comparison in the Mesosphere-Lower Thermosphere, *Journal of Geophysical Research Atmospheres*, Manuscript 2017JD027454

Whiteway, J. A., Carswell, A. I., & Ward, W. E. (1995), Mesospheric temperature inversions with overlying nearly adiabatic lapse rate: an indication of a well-mixed turbulent layer, *Geophysical Research Lett*ers, *22*(10), 1201-1204. https://doi:10.1029/95GL01109

Wickwar, V. B., Beissner, K. C., Wilkerson, T. D., Collins, S. C., Maloney, J. M., Meriwether, J. W. Jr., & Gao, X. (1997), Climatology of Mesospheric Temperature Profiles Observed with the Consortium Rayleigh-Scatter Lidar at Logan, Utah, In *Advances in Atmospheric Remote Sensing with Lidar*, A. Ansmann, R. Neuber, P. Rairoux, & U. Wandinger (Eds.), 557-560, Springer, Berlin. https://doi:10.1007/978-3-642-60612-0

Wickwar, V. B., Wilkerson, T. D., Hammond, M., & Herron J. P. (2001), Mesospheric temperature observations at the USU / CASS Atmospheric Lidar Observatory (ALO), In *Remote Sensing of the Atmosphere, Environment, and Space,* U. N. Singh, T. Itabe, & N. Sugimoto (Eds.), *Proceedings of SPIE*, *4153*, 272–284. https://doi:10.1117/12.417056

Wickwar, V. B., Taylor, M. J., Herron, J. P., & Martineau, B. A. (2002), Visual and lidar observations of noctilucent clouds above Logan, Utah, at 41.7° N, *Journal of Geophysical Research*, *107*(D7), 4054. https://doi:10.1029/2001JD002280

Wickwar, V. B., Sox, L., Emerick, M. T., Herron, J. P., & Barton, D. L. (2016), Early Observations with the Extremely Sensitive Rayleigh Lidar at Utah State University, *EPJ Web of Conferences*, *119*, 13007. https://doi:10.1051/epjconf/201611913007

Wynn, T. A. (2010). Statistical analysis of the USU lidar data set with reference to mesospheric solar response and cooling rate calculation, with analysis of statistical issues affecting the regression coefficients, (Doctoral dissertation). Retrieved from (http://digitalcommons.usu.edu/etd/797). Logan, UT: Utah State University.